

**Resolution Limits and Process Latitude of  
Conformable Contact Nano-Lithography**

by

Corey Patrick Fucetola

S.B. Mathematics, M.I.T., 2004; S.B. EECS, M.I.T., 2005

Submitted to the Department of Electrical Engineering and Computer Science

in Partial Fulfillment of the Requirements for the Degree of

Master of Engineering in Electrical Engineering and Computer Science


at the Massachusetts Institute of Technology

February 2007

©2007 Corey Fucetola. All rights reserved.


The author hereby grants to MIT permission to reproduce and to distribute publicly paper and electronic copies of the thesis document in whole or in part.

Signature of Author \_\_\_\_\_

 Department of Electrical Engineering and Computer Science

October 11, 2006

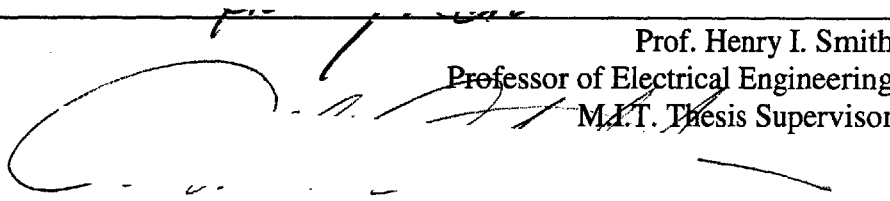
Certified by \_\_\_\_\_

 David J. Carter

Charles Stark Draper Laboratory

Thesis Supervisor

Certified by \_\_\_\_\_

 Prof. Henry I. Smith

Professor of Electrical Engineering

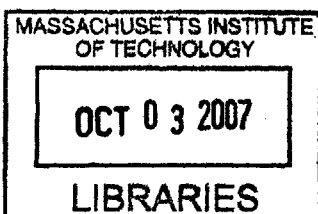
M.I.T. Thesis Supervisor

Accepted by \_\_\_\_\_

Arthur C. Smith

Professor of Electrical Engineering

Chairman, Department Committee on Graduate Theses



ARCHIVES

[THIS PAGE INTENTIONALLY LEFT BLANK]

# **Resolution Limits and Process Latitude of Conformable Contact Nano-Lithography**

by  
Corey P. Fucetola

Submitted to the  
Department of Electrical Engineering and Computer Science on

October 13, 2006,

In partial fulfillment of the requirements for the Degree of  
Masters of Engineering in Electrical Engineering and Computer Science

## **Abstract**

Conformable Contact Lithography enables researchers to attain high-resolution lithographic patterning at manageable cost. This thesis characterizes the minimum resolvable feature size and process latitude of Conformable Contact Lithography.

Beginning with a review of current lithographic patterning techniques, choice of Conformable Contract Lithography as an exposure technique is discussed. A design for a trilayer stack that optimizes optical properties is established using experimental and simulated reflectance data to choose appropriate stack film thicknesses. The simulated process latitude is constructed using electromagnetic simulations of grating patterns. Image analysis of experimentally-exposed diffraction grating patterns is described and used to characterize the effect of exposure dose on printed linewidth. The resulting simulated and experimental process latitudes for printed gratings are presented for masks utilizing protruding chrome lines and embedded chrome lines.

Experimental and simulated reflectance for single-layer and bilayer film stacks are compared to yield an optimized trilayer stack design of 225nm of anti-reflection-coating chemically separated from the resist by 70nm of evaporated silicon oxide. This design results in less than 1.5% back-reflection from the oxide into the resist for 10% film thickness variation.

Finite-difference time-domain simulations are optimized by comparing higher variable-resolution, more realistic simulations to more efficient, lower variable-resolution simulations. Building on the trilayer stack and optimal simulation specification, simulated exposures of diffraction gratings are analyzed assuming a clipping model of development.

Exposures of dense grating patterns with two geometries are performed on trilayer-stack-coated silicon wafers for a range of doses. Transferred grating patterns are analyzed to establish the effect of exposure dose on printed linewidth.

A 5% experimental process latitude is achieved at a printed linewidth tolerance of  $\pm 15\%$  for the embedded chrome mask exposures and of 25% for the protruding chrome mask exposures. Within the resist, contrast is higher at smaller gratings using the embedded mask.

Technical Supervisor: Dr. David J. Carter  
Title: Principal Member of the Technical Staff, Draper Laboratory

Thesis Advisor: Professor Henry I. Smith  
Title: Professor of Electrical Engineering

[THIS PAGE INTENTIONALLY LEFT BLANK]

## Acknowledgements

October, 11, 2006

This thesis was made possible through the support of many and the dedication of a few.

My mother and father deserve more credit than I can ever adequately acknowledge. Their support, critiques and care packages certainly sustained my effort throughout. I am also extremely fortunate to have a brother capable of recasting my overwhelming trepidations into surmountable challenges.

David Carter, my supervisor, gave me courage to continue – time and time again. His dedication inspired me to continue writing, analyzing and revising my results until their presentation became both accurate and clear. James Goodbelet, from LilCo Inc., enabled the final experimental study. Without his timely provision of two masks, the exposure study presented within would not have been possible. Joe Ricker, from Draper Laboratory, deserves acknowledgement for providing several hundred beautiful images to analyze for the exposure study. Connie Cardoso, Dan Pulver and Mark April, all part of the Draper Laboratory MEMS group were extremely helpful throughout my work in the clean room. Whether it was giving me tools, chemicals or a simple pat-on-the-back they were always accessible, helpful and insightful.

I cannot thank you all enough for your help in helping make this thesis an enlightening and enjoyable experience.

This thesis was prepared at The Charles Stark Draper Laboratory, Inc., under Independent Research and Development: Nanoscale Fabrication with Applications and Carbon Nanotube Device Development, Con-05000-2

Publication of this thesis does not constitute approval by Draper or the sponsoring agency of the findings or conclusions contained herein. It is published for the exchange and stimulation of ideas.

---

Corey Fucetola

[THIS PAGE INTENTIONALLY LEFT BLANK]

## CONTENTS

Abstract .....	3
I. Introduction.....	9
1. Background: Micro- and Nano-Processing 101.....	9
a. The Planar Fabrication Process.....	9
b. Current Patterning Systems and Processes .....	10
c. The Experimental Environment.....	14
d. The Software Programs.....	16
2. Nano-processing at Draper Laboratory.....	17
a. Running the LilCo CCL System.....	17
b. The Optical Path: from source to substrate.....	18
c. The Mask .....	20
d. Developing the DUV Photoresist.....	21
e. Stack Engineering to Reduce Back Reflections.....	22
3. Scope.....	23
II. Film Stack optimization.....	24
1. Designing the Trilayer Stack: film by film.....	25
2. The thickness and reflectance of deposited monolayer SiO <sub>2</sub> and ARC films are compared to simulated monolayer films.....	25
3. The thickness and reflectance of evaporated SiO <sub>2</sub> coated ARC films are compared to simulated bilayer film stacks.....	27
4. The simulations predict interlayer thicknesses of the trilayer stack .....	28
III. Intensity Simulations .....	30
1. E-M Suite Optimizations .....	30
a. Memory Requirements and Running time.....	32
b. EM-Suite Environment.....	33
2. EM-Suite Simulations.....	37
a. Simulated Linewidth Measurements.....	41
b. Linewidth measurement limitations.....	43
c. Linewidth vs. Intensity and Dose.....	44
IV. Linewidth vs Dose .....	46
1. Experiment: expose wafers at different doses using both masks.....	48
2. EAM exposures.....	50
3. SCM Exposures .....	54
V. Linewidth vs Dose Analysis .....	57
1. Simulation Results .....	57
2. Experimental results.....	61
VI. Contributions.....	66
VII. APPENDIX.....	67
1. Appendix 1: Single Exposure Printing Procedure (adapted from [22]).....	67
2. Appendix 2: Simulations of the trilayer stack.....	70
3. List of Figures and Tables.....	73
4. REFERENCES .....	78

[THIS PAGE INTENTIONALLY LEFT BLANK]



## **I. Introduction**

The vast majority of micro- and nanoscale devices fabricated today use the planar fabrication process. Silicon wafers and other substrates undergoing planar fabrication are successively morphed into devices as material film layers are selected, cleared, added or removed from the wafer surface. A critical component of almost all of these steps is lithographic patterning, which is achieved through a variety of technologies detailed below. Of particular interest is conformable-contact lithography (CCL), a low-cost, high-resolution patterning technique suitable for research and low-level production. This thesis aims to establish the resolution limits for CCL through an experimental study supported by simulations of the linewidth produced with CCL.

### **1. Background: Micro- and Nano-Processing 101**

The necessary background will now be provided before establishing the resolution limits for CCL. A brief review of various types of lithographic fabrication processes motivates the choice of our lithography system. After introducing the lithographic process, the experimental tools are described, and lastly, the simulation software is outlined.

#### **a. The Planar Fabrication Process**

The planar fabrication process requires first transferring a pattern to resist followed by chemical or physical processing to act upon the transferred pattern. In the CCL exposure system, emitted radiation passes through a series of filtering mirrors and lenses to become incident upon a mask. The mask partially transmits light, implanting energy and a latent pattern into the resist. The patterned resist film absorbs the energy passing through the mask, changing its chemical selectivity so that – in the case of a positive resist – the exposed area dissolves in developer.

## The Planar Fabrication Process

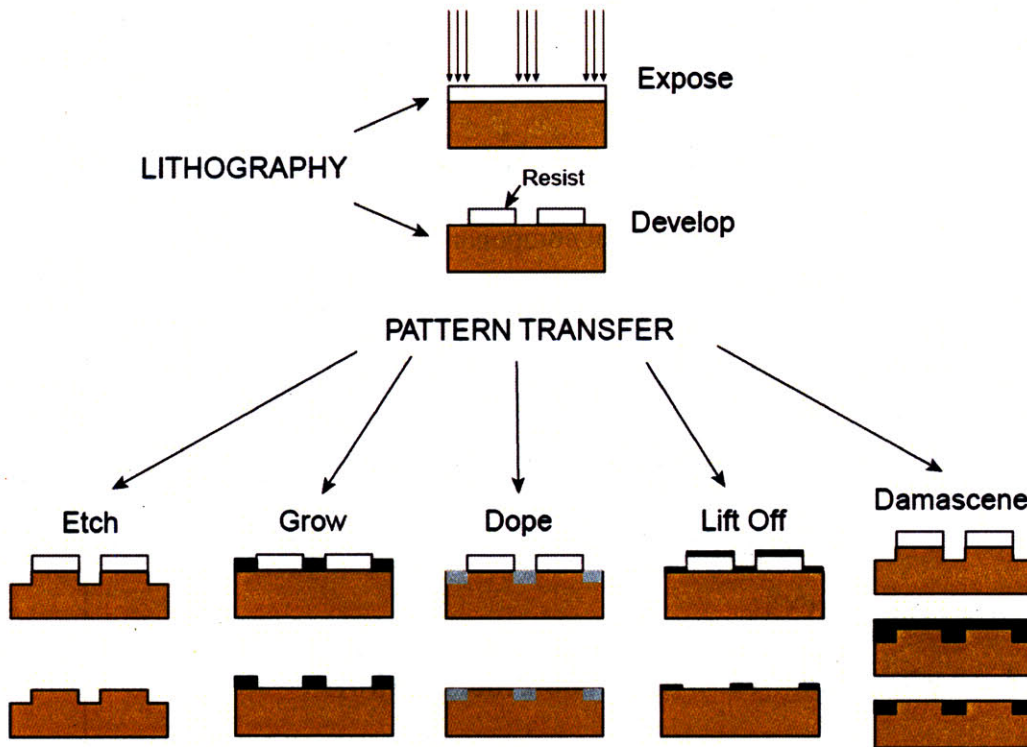


FIGURE I.1: THE PLANAR FABRICATION PROCESS. DURING THE LITHOGRAPHIC STEP REGIONS OF EXPOSED RESIST ARE CLEARED DURING DEVELOPMENT. AFTER THE LITHOGRAPHIC STEP, THE PATTERNED RESIST UNDERGOES FURTHER PROCESSING.

Developing the resist completes the lithographic component of the planar fabrication process. The undesired regions in the resist film are cleared in a solution and the wafer is rinsed clean of developer. Cleared patterns expose films underneath the resist that are candidate locations for deposition and etching through chemical or physical processing. If, after deposition or etching, further processing with a new pattern is required, the planar fabrication process continues with another lithographic step.

### b. Current Patterning Systems and Processes

The lithographic patterning step typically limits device density and minimum feature size. Furthermore, systems providing pattern transfer are an integral part of the fabrication process and must be cost-effective. Focusing on high-volume production, the semiconductor industry has

been driven to maximize device density [1] and increase wafer size. As a result, commercially-produced integrated circuits utilize projection-lithography systems to expose wafers during pattern transfer steps. These systems require large capital investment but allow for high-volume production and excellent resolution and reproducibility. The large capital investment necessary to obtain projection equipment is mitigated by the high-volume production inherent to this industry. However, a research community targeted at lower-volume production is prohibited from adopting these systems due to the large required capital investment.

Nanofabrication in research settings typically does not require high throughput, and is often sensitive to large capital and design costs. Contact lithography, imprint lithography, soft lithography, X-ray lithography, electron-beam lithography and Conformable Contact Lithography (CCL) are some of the pattern transfer processes utilized in research-focused communities. Contact lithography, X-ray lithography and CCL utilize photons to preferentially pattern a substrate using a mask. In contrast, imprint lithography and soft lithography require pre-fabricated master patterns that are then mechanically transferred to various substrates. For these types of applications, electron-beam lithography provides cost-effective high-resolution patterning capabilities sufficient to create either the mask or the master. Electron-beam lithography is also used for low-volume, high-resolution direct-write fabrication of devices. The following is a brief description of these different pattern transfer processes in terms of resolution and registration.

Contact lithography provides moderate yield and throughput. Using the i-line spectrum from an Hg arc lamp [2, 3], it has been the primary technique for printing linewidths down to  $\sim 1$   $\mu\text{m}$  in research laboratories for many years. The resolution of contact lithography is limited by near-field diffraction and can be increased by utilizing sources that provide shorter wavelengths.

To this end, various sources have been adopted including Xe-Hg arc lamps [3, 4, 5], ArF excimer lasers [6] and F<sub>2</sub> excimer lasers [7].

Smaller mask-to-substrate gaps also improve resolution in contact lithography [8]; proximity printing, soft contact printing, and vacuum printing offer progressively better mask-to-substrate contact at the potential expense of degradation of the mask resulting from mechanical wear during hard contact to the substrate. However, decreasing the gap between the mask and substrate can be difficult. Wafer flatness, particles, resist edge bead and surface structures on the wafer [9, 10] generate locally distributed spacing at the mask-substrate interface, which in turn decrease pattern resolution. Furthermore, gaps may also be introduced as a result of trapped or generated gases [5, 11]. Contact lithography can have limited registration, or alignment, across multiple masked processes due to mechanical slippage occurring when vacuum is applied to sequential masks, [12].

The techniques of imprint lithography, soft lithography, X-ray lithography and electron-beam lithography obtain better resolution than contact lithography, but have their own inherent shortcomings.

Imprint Lithography uses prefabricated master templates with the patterns defined topographically; pressure is applied to the master forcing a heated liquid polymer to conform to the master, and the temperature is decreased until the liquid solidifies. As mentioned, generally the lithographic process that is used to create the master stamp limits this technique's resolution. In this process, registration problems exist with multiple layered patterns due to the liquid phase of the polymer [13].

Soft lithographic templates result from curing a polymeric solution (typically PDMS) applied to master substrates that have previously undergone the patterning process. Similar to

imprint lithography, this technique is limited in resolution by the master mask. The cured polymeric 'stamp' is used to mechanically transfer a chemical pattern to the substrate. Problematically, it is a process that is chemically complex, requires Au or Ag masking materials, contains significant defects and poses difficulties in registration [14].

X-ray lithography, based on using X-ray sources [5, 15] to obtain pattern transfer, provides good resolution but requires complicated exposure systems, such as a synchrotron, to achieve moderate throughput [13]. Electron-beam lithography [5] is capable of extremely high resolution, but has a very a low throughput. This process is limited in its resolution by scattered electrons resulting when the primary beam strikes the substrate.

CCL, an extension of contact lithography, typically operates in the i-line spectrum or deep-ultra-violet (DUV) spectrum of a XeHg lamp, though laser sources are also used. CCL differs from contact lithography: by using a flexible mask [12, 16, 17, 18] local gaps between the mask and substrate are minimized. Additionally, optically-optimized material stacks [2, 3, 5, 6] are used to control reflections from resist interfaces, thereby increasing the resolution. Of particular interest is a trilayer stack configuration consisting of an oxide layer beneath the resist and above an anti-reflection coating (ARC). This configuration minimizes undesirable reflections that degrade optical image quality. Also, the trilayer resist provides a processing buffer between the resist and substrate. Another extension that minimizes the gap and decreases mask degradation is an Embedded Amplitude Mask (EAM) [19, 20, 21]. These masks can be engineered to provide a better match between the optical properties of the mask and resist, potentially extending the resolution to smaller linewidths. Due to vacuum printing and the conformability of the mask, CCL almost always provides better resolution than contact

lithography. However, its resolution is still limited by exposure wavelength and there is a potential for mask degradation.

CCL is capable of bridging the processing gap between commercially-used techniques and those used by research institutions. The issue of registration between multiple masks is under current investigation [22] but does not apply to the single masked exposures considered in this thesis.

### c. The Experimental Environment

The LilCo CCL System [23] will be used throughout this thesis and is comprised of a deep-UV (DUV) mercury arc light source, stage, pneumatic controller, and optics controller (Figure I.2). The light source contains a XeHg-arc Lamp source, two mirrors and a collimating lens. The stage is a movable open chamber, which when appropriately loaded with a wafer and mask can be evacuated to provide intimate contact at the wafer-to-mask interface. The stage positioning is controlled with LabView. Stage motion to and from the light source, vacuum between the wafer and stage, and contact between the mask and wafer are controlled pneumatically. The optics controller initiates and terminates wafer exposures by opening or closing a shutter. The lamp power supply sustains the output power of the light source at 22 mW/cm<sup>2</sup>.

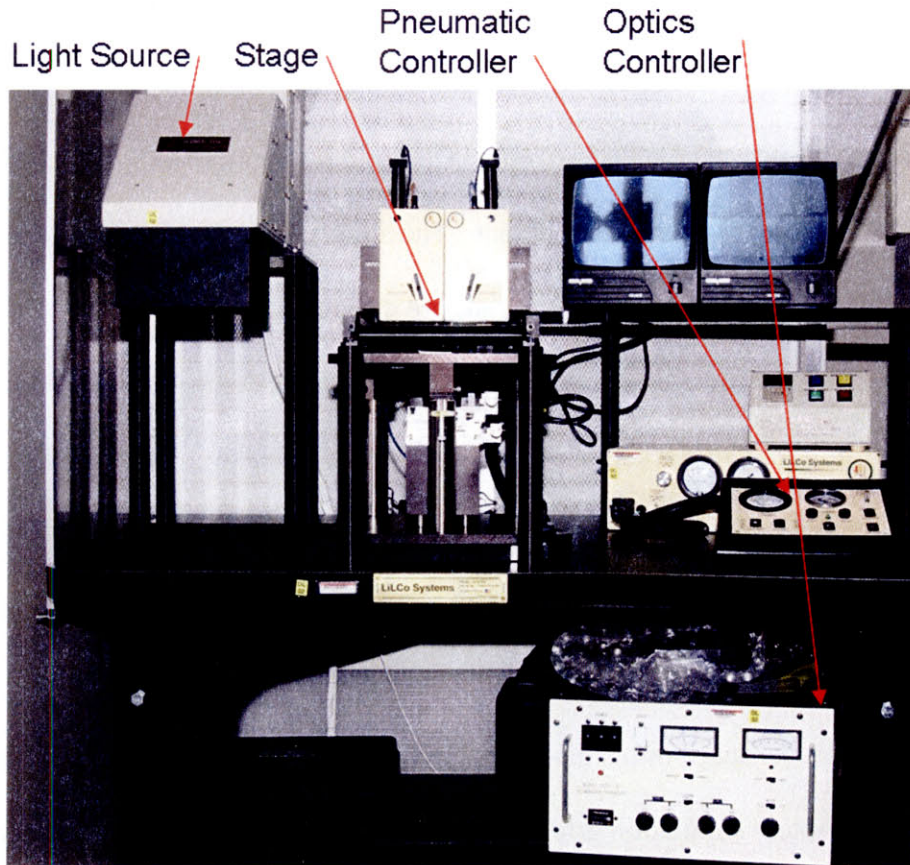


FIGURE I.2: THE LILCo CCL ALIGNER AT DRAPER LABORATORY. ARROWS INDICATE THE LOCATIONS OF THE LIGHT SOURCE, STAGE, PNEUMATIC CONTROLLER AND OPTICS CONTROLLER.

After exposure, 950kD Poly-Methyl-Methacrylate (PMMA)-coated wafers undergo development in a bath of 1-part Methyl Isobutyl Ketone (MIBK) to 2-parts Isopropanol (IPA) for 60 seconds. Developer temperature is controlled to within  $1^{\circ}\text{C}$  of  $20^{\circ}\text{C}$  using a recirculating bath. After development, wafers are rinsed in isopropyl alcohol (IPA) for 60s.

After development the wafers are examined and characterized. The hardware used to characterize the wafers considered in this thesis includes an atomic force microscope (AFM), scanning-electron microscope (SEM), ellipsometer, and UV-Visible spectrophotometer (UV-vis). In addition, some software tools have been developed for simulation and data characterization, which will now be described.

#### d. The Software Programs

EM-Suite, Panoramic Technology's finite-difference time-domain (FDTD) Maxwell's equation modeler (based on TEMPEST from U.C. Berkeley), numerically solves Maxwell's equations throughout a simulated environment. The simulation environment is configured using a list of discrete variables and relevant materials are defined using their complex indices of refraction. Various simulators exist in EM-Suite to numerically constrain electro-magnetic and chemical behavior: index of refraction models support intensity simulators while dissolution rate models enable the resist development simulator. In this thesis, simulators are used to predict reflectance at the top of a stack of materials, and optical intensity profiles of two-dimensional environments<sup>1</sup>.

EM-Suite breaks space into a discrete simulation grid defined from within the environmental variables (simulation grid, number of exposure wavelengths, number of exposure source angles, ...). Increasing the number of variable values in a simulator's environment requires longer simulator runs while too few variable values degrades modeling accuracy. Targeting the proper level of discretization for these variables is detailed in Chapter III.

When necessary, Matlab was used to provide additional numerical insight not supported by the Panoramic software. Finally, analysis of SEM images, accomplished using Image Pro image analysis software, established the linewidth,  $\mathcal{L}$ , of experimental grating exposures for a variety of exposure doses.

---

<sup>1</sup> During the course of the thesis, an attempt was made to model the dissolution rate of PMMA irradiated by the DUV spectrum. Had the dissolution rate been determined experimentally, EM-Suite would have been able to model resist development of grating exposures. The approach to modeling PMMA development was not included because experimental limitations prohibited determination of an accurate model.



## 2. Nano-processing at Draper Laboratory

The short-wavelength deep-ultra-violet (DUV) spectrum of the Xe-Hg lamp is preferred to resolve the finest features. The direct reduction in feature size resulting from using short wavelengths is desirable, and targeting these short wavelengths is achieved by proper choice of arc-discharge lamp and mirror sets (which filter the spectrum) in the light source.

Previously, in I.1.c and I.1.d, a brief description of the LilCo CCL system and supporting simulations tools were provided. Operation of the LilCo CCL system is described here, though a complete standard operating procedure (SOP) is included in Appendix 1. Following this, the optics between the lamp and substrate are discussed. Next, the photoresist and the methodology used to design the trilayer stack are described.

### a. Running the LilCo CCL System

Operation of the LilCo system is simple for unmasked (flood) exposures. After measuring the incident power striking the wafer chuck, the stage is moved from underneath the light source to the alignment station. Once there, a wafer is placed flat-down in the center of the stage and held by a vacuum applied to its backside. Then, the stage is moved back under the light source and illuminated for a predetermined amount of time.

Involving a pattern transfer mask adds the critical step of contact to the CCL system operation. When the mask and wafer are brought close enough together a vacuum is drawn, creating intimate contact between the two [24]. The region of contact between the mask and wafer is sensitive to the parallelization of the mask and the wafer and carefully leveling the wafer – by centering the initial point of contact – increases this area. Furthermore, air bubbles surrounding particles can be released by increasing the vacuum *very* slowly. Once in hard

contact, the stage is moved underneath the light source where DUV radiation is emitted for a programmed time.

b. The Optical Path: from source to substrate

The optical path within the light source determines what wavelengths from the Xe-Hg lamp spectrum are most pronounced at the mask-wafer interface. Limits in minimum resolvable feature depend directly on the wavelength of irradiation, so engineering the optical spectrum incident at the mask-wafer interface is crucial to resolving small features [22, 25, 26].

The LilCo System comprises of two subsystems: the light source and the stage. Within the light source, the Xe-Hg lamp spectrum is reflected off two mirrors and sent through two lenses, becoming collimated to within  $\pm 2$  degrees from perpendicular, and travels through a mask to impinge upon the substrate surface. This light diffracts through the mask and is absorbed by the resist.

More specifically, light initiated at the Xe-Hg source is filtered by the reflection characteristics of each of the mirrors, refracted at the fly's-eye and collimating lenses according to Snell's Law, diffracted through the mask and, lastly, absorbed by the resist. The absorption within the resist indicates the relevant range of wavelengths that needs to be considered (*i.e.* discretized) in simulations. Figure I.3 shows the spectrum from the lamp (green line), after two mirror bounces (crosshatched green line), and multiplied by PMMA absorption (blue line), along with a discretization of 30 wavelengths or bins (blue circles) over the wavelength range from 200-260 nm.

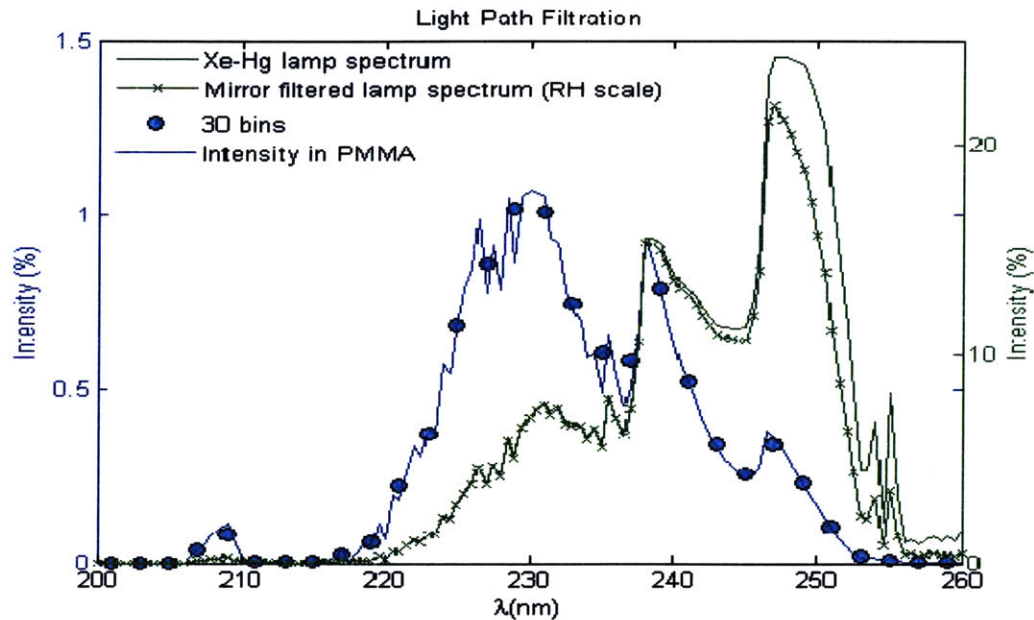


FIGURE I.3: THE XE-HG-ARC LAMP SPECTRUM AS IT PROPAGATES THROUGH THE CCL OPTICAL SYSTEM. AS THE XE-HG SPECTRUM (SOLID GREEN LINE) IS FILTERED BY MIRRORS (GREEN LINE WITH X'S), THE INTENSITY PROFILE DISPROPORTIONALLY DECREASES IN THE LONGER WAVELENGTHS (INCLUDING THOSE BEYOND THE UPPER LIMIT OF THIS PLOT), ISOLATING THE DUV SPECTRUM FOR EXPOSURES. THE INCIDENT INTENSITY SPECTRUM MULTIPLIED BY PMMA ABSORPTION (BLUE LINE) IS SHOWN ON THE LEFTHAND SCALE AND IS DISCRETIZED INTO 30 BINS, OR SPECTRAL PAIRS. THE INTEGRATED XE-HG SPECTRUM IS NORMALIZED TO 1.

It should be noted that the PMMA absorption (derived from the imaginary component of the index of refraction) tracks the measured PMMA sensitivity in the DUV wavelength range of 200-260 nm [3]. This wavelength range is experimentally relevant; Mimura [3] reports no sensitivity above 260 nm, and below 200 nm UV radiation is absorbed by ambient oxygen.

The DUV spectrum, filtered from the Xe-Hg lamp, is emitted from the light source and becomes incident on the surface of the mask. This spectrum then exposes the resist underneath the mask, implanting a dose of energy proportional to the integrated intensity,  $I_0$ , within the PMMA. The dose of energy,  $D_0$ , is equal to  $I_0$  scaled by the length of time the mask and wafer are illuminated. One notable attribute the DUV spectrum is its lack of well-defined peaks, which has consequences for the simulations discussed in Chapter III.

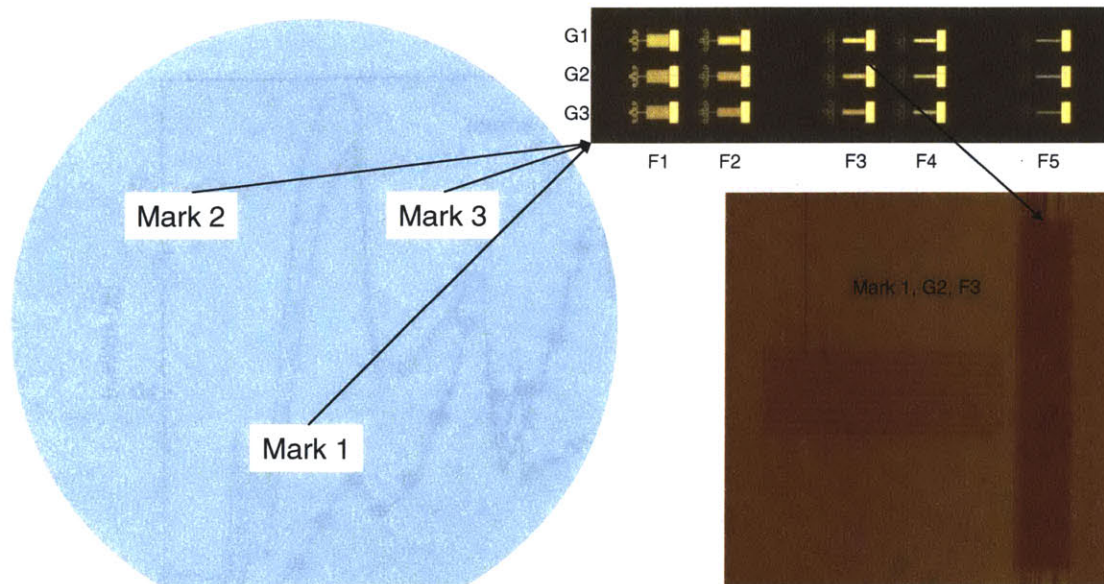


FIGURE I.4: THE LAYOUT OF THE MASK. REGIONS MARK 1, MARK 2 AND MARK 3 EACH CONTAIN THE 15 GRATINGS IN THE UPPER RIGHT. IN THE LOWER RIGHT IS THE FIRST GRATING (G2) FOR THE PITCH OF F3. IN THE MATRIX OF GRATINGS IN THE UPPER RIGHT, THE ROWS VARY IN E-BEAM EXPOSURE DOSE: G1=+15%, G2=0% AND G3=-15% (PERCENTAGES REPRESENT OVER- OR UNDEREXPOSURE FROM NOMINAL 1:1 DUTY CYCLE). THE COLUMNS VARY IN PITCH WITH F1=1000NM, F2=700NM, F3=400NM, F4=300NM AND F5=200NM.

### c. The Mask

In general, analysis of an arbitrary lithographic pattern exposure can be rather complicated, however, dense gratings and isolated lines can serve as representative structures for the purpose of analysis of resolution and process latitude.

A clear-field embedded amplitude mask (EAM) [19, 20, 21] and dark-field standard chrome mask (SCM) were provided, courtesy of James Goodberlet of LilCo, to enable the process latitude experiment. Each mask contains dense and isolated features; the clear-field mask was predominantly fused-silica with masking chrome lines whereas the dark-field mask was substantially chrome-coated with transmitting fused silica apertures. The absorbing chrome lines are recessed into the mask for the EAM and protrude out from the mask for the SCM. Diffraction gratings, created by chromium liftoff after electron-beam lithography, are specified in linewidth and pitch. The mask is designed with three repeated marks, each comprising fifteen diffraction gratings. Within each group of fifteen gratings are targeted five different pitches each

with three different electron-beam-written duty cycles varying in target linewidth from 500nm to 100nm (Figure I.4).

Table I.a shows linewidths measured from SEM images of one set of marks on the SCM, and multiple marks on the EAM.

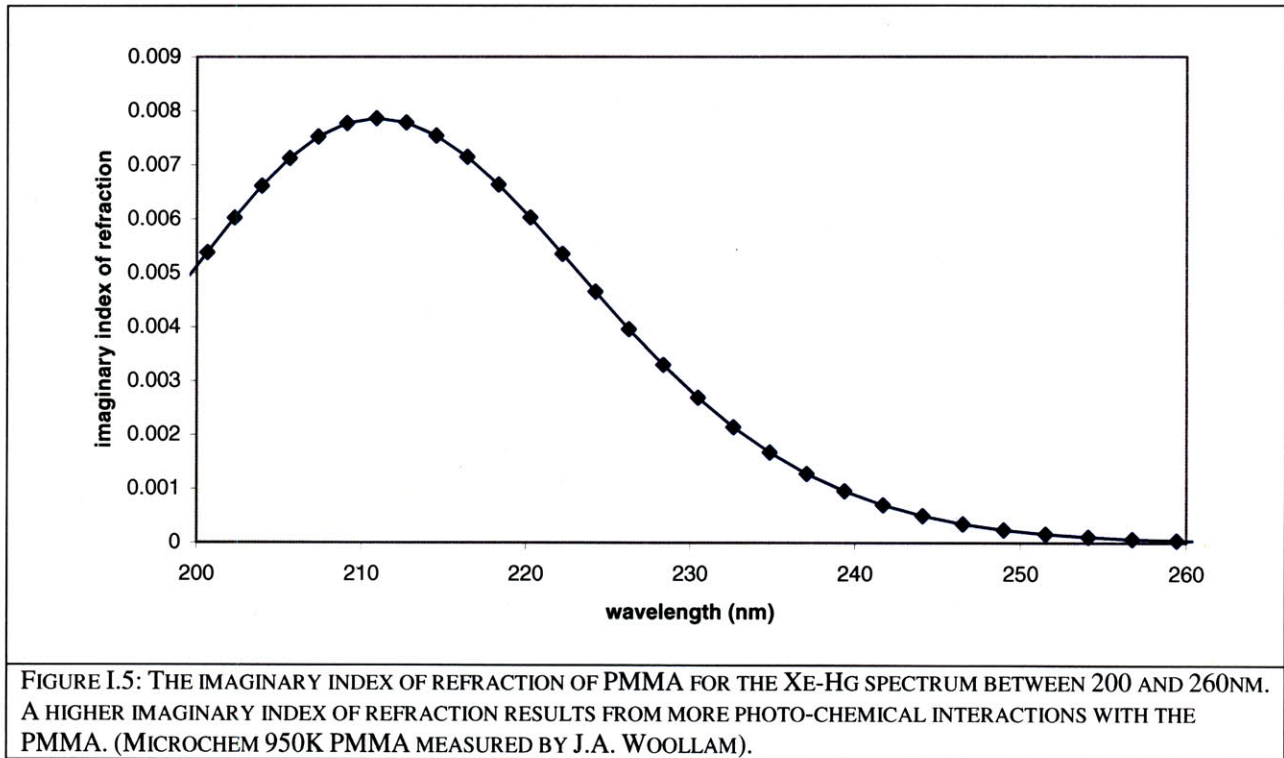
<i>Design period</i>	<i>Dose</i>	<i>Measured linewidth</i>	
		<b>EAM</b>	<b>SCM</b>
1000	1	593	
1000	2	576	425
1000	3	560	
700	1	452	
700	2	425	277
700	3	408	
400	1	270	
400	2	254	167
400	3	239	
300	1	205	
300	2	193	123
300	3	183	
200	1	145	
200	2	138	89
200	3	127	

TABLE I.a: MEASURED LINewidthS FOR CCL MASKS USED IN THIS THESIS. ONE MARK SET PER MASK WAS IMAGED WITH A SCANNING-ELECTRON MICROSCOPE, AND LINewidthS WERE MEASURED MANUALLY FROM THE SEM IMAGE.

#### d. Developing the DUV Photoresist

Beneath the mask is first a layer of photoresist, which is potentially followed by other film layers. The positive resist, PMMA, has been found to be an excellent DUV resist insofar as it absorbs light primarily in this modified Xe-Hg spectrum and is transparent to light that is above 300nm [2, 5, 6]. Shown in Figure I.5 is the PMMA imaginary index of refraction over the DUV range, 200nm to 260nm, indicating absorption in this wavelength range. Mimura *et al.*

experimentally determined the PMMA sensitivity for DUV exposures [3], which tracks the absorption (shown in Figure I.5) as measured by Wollam *et al.*



The mechanism for degradation of the PMMA under DUV irradiation has been studied extensively elsewhere and results from chain scissioned ester bonds [2, 3, 4, 5]. Acting as the developer, a mixture of 1 part MIBK to 2 parts IPA at 20°C dissolves PMMA with a dissolution rate model related to the dose of implanted energy approximately cubed [27].

#### e. Stack Engineering to Reduce Back Reflections

Exposing a wafer at a given power density for a known amount of time deposits energy into the photoresist. One of the mechanisms to control intensity profiles within the PMMA is to eliminate back reflections from the bottom resist surface using a trilayer stack [28]. By carefully selecting underlying films, the forward-propagating electro-magnetic wave contributes nearly all of the deposited energy within the resist [6]. At the interface between the resist and the

underlying material exists an ensemble reflection and transmission coefficient resulting from a geometric sum of waveforms [29]. By choosing the films' thicknesses correctly, the ensemble reflection back into the PMMA resist is minimized.

### **3. Scope**

The remainder of the thesis will detail the optimization of a trilayer film stack for DUV CCL, discuss and present simulations of CCL exposures, present experimental CCL exposures, and compare experiment to simulation.

In Chapter II, reflectance data collected from a UV-visible spectrophotometer on wafers coated with trilayer-stack component materials is used as a comparison to simulated reflectance. A good comparison between the simulated and experimental data will verify simulations, which will then be used to determine the optimum film thicknesses of the trilayer stack between the mask and silicon wafer.

In Chapter III, the procedure used for optimizing exposure-simulation throughput and accuracy are detailed. Simulations of CCL exposures with varying linewidth, resist stack and mask configuration are then presented.

The experimental CCL exposures using SCM and EAM masks are discussed in Chapter IV. The experimental methods for exposure, development, imaging, and analysis are detailed.

Chapter V compares the experimental and simulated exposures, and uses these results to discuss the resolution limits and process latitude of conformable-contact lithography.

In Appendix 1 is the LilCo SOP. In Appendix 2 are exploratory simulations that provide qualitative insight about the given PMMA resist thickness and masking chrome thickness.

## II. Film Stack optimization

At an interface between materials of differing indices of refraction, incident light is reflected and transmitted. Within an optical photoresist, reflected light waves constructively and destructively interfere with incident light waves creating nodes and anti-nodes of intensity. If the reflection is too strong it can impact the successful replication of features: developing the exposed resist will proceed quickly through the nodes and slowly through the anti-nodes, and the linewidth will be sensitive to the underlying material on the substrate (for example higher reflectance would be expected over a metal line than over a bare silicon surface). Within the resist, decreasing the reflection minimizes these deleterious effects, potentially enabling resolution of smaller features.

For CCL, an optical stack, consisting of an absorbing polymer (anti-reflection coating or ARC) and a layer of silicon oxide<sup>(2)</sup> is deposited under the PMMA resist to minimize reflection back into the resist and to chemically separate the ARC and PMMA. Designed below in section II.4, the trilayer stack's constituent film thicknesses will reduce reflections from the resist-oxide interface. The XHri-C-ARC was obtained from Brewer Science and the PMMA was obtained from Microchem<sup>(3)</sup>.

A trilayer stack is built on the silicon wafers for two reasons. First, minimizing the reflectance within the resist by optimizing the ARC and SiO<sub>2</sub> thicknesses improves the uniformity of the intensity profile [6], and therefore, improves the development profile of the resist. Second, this configuration allows for a thin imaging layer (the PMMA) to preserve

---

<sup>(2)</sup> Technically, the evaporated oxide is SiO<sub>x</sub> rather than SiO<sub>2</sub>. However in this thesis SiO<sub>2</sub> is used to indicate evaporated SiO<sub>x</sub>.

<sup>(3)</sup> J.A. Woollam measured the index of refraction for SiO<sub>x</sub> and ARC, and PMMA.



feature replication, which can be transferred into the underlying layers (and ultimately the substrate) because of the chemical selectivity between the stack layers [6].

### **1. Designing the Trilayer Stack: film by film**

In simple configurations PMMA, or another resist material, is the only film deposited on the substrate. However, more complicated (bilayer and trilayer) stacks contain ARC and SiO<sub>2</sub> layers deposited on top of the silicon wafer. In our experiments, deposited film thickness was measured on an ellipsometer or surface profilometer.

In the following, single-film measurements are first compared to simulations, thus validating the simple simulations and index-of-refraction data. Then, a series of wafers with bilayer stacks are experimentally characterized and simulated, providing further comparison and validation of multilayer simulations. Finally, PMMA is added to the bilayer stack simulation and the optimal target thicknesses of ARC and SiO<sub>2</sub> for DUV CCL exposures are predicted.

### **2. The thickness and reflectance of deposited monolayer SiO<sub>2</sub> and ARC films are compared to simulated monolayer films.**

As an experimental starting point to validate our simulation capabilities and the index of refraction data, silicon wafers were coated with SiO<sub>2</sub> or ARC. Their reflectance was measured over the wavelength range of 200nm to 300nm.

A single-film structure was simulated using the ellipsometer-measured film thicknesses and index of refraction data. The RMS error was then calculated between the characterized and simulated reflectance. The reflectance is plotted for the SiO<sub>2</sub> films (Figure II.1), and for the ARC films (Figure II.2) over the span of wavelengths from 200nm to 300nm.

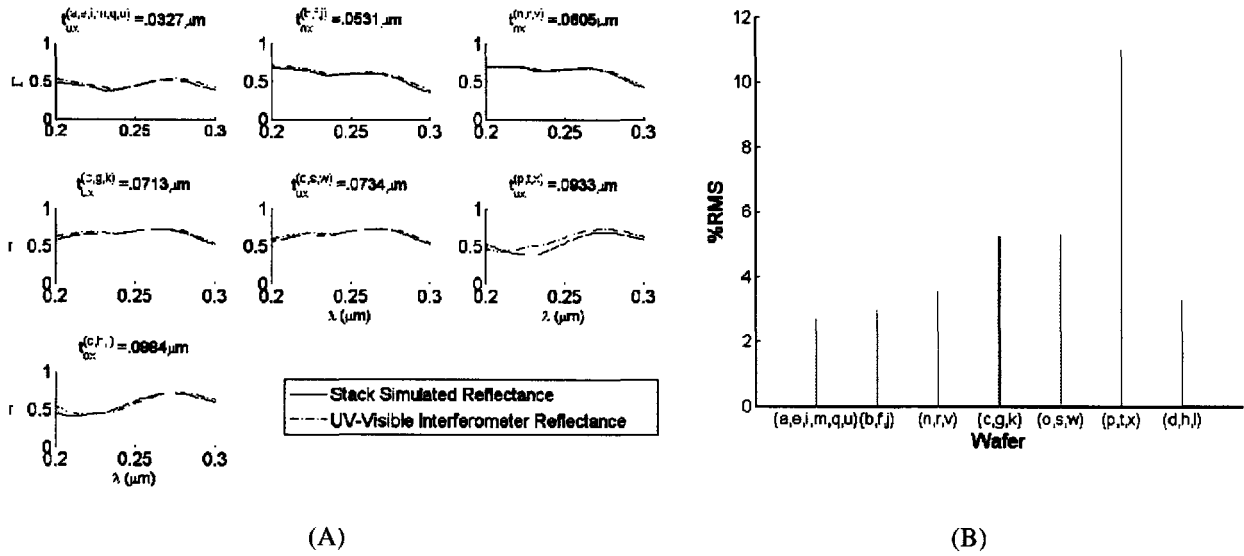


FIGURE II.1: (A) REFLECTANCE VS WAVELENGTH PLOTS FOR FILMS OF  $\text{SiO}_2$  (THICKNESS RANGED OVER 32NM TO 98NM) EVAPORATED ONTO A SILICON WAFER. THE SIMULATED (DOTTED) AND MEASURED (SOLID) REFLECTANCE CURVES ARE COMPARED IN (B). (B) RMS ERRORS FOR EACH  $\text{SiO}_2$  COATED WAFER IS CALCULATED BETWEEN THE EXPERIMENTAL AND SIMULATED REFLECTANCE CURVES. NOTE THAT THE ERROR BETWEEN SIMULATION AND EXPERIMENT WAS TYPICALLY LESS THAN 5% (WITH THE EXCEPTION OF ONE WAFER, WHERE THICKNESS MEASUREMENT ERROR IS SUSPECTED).

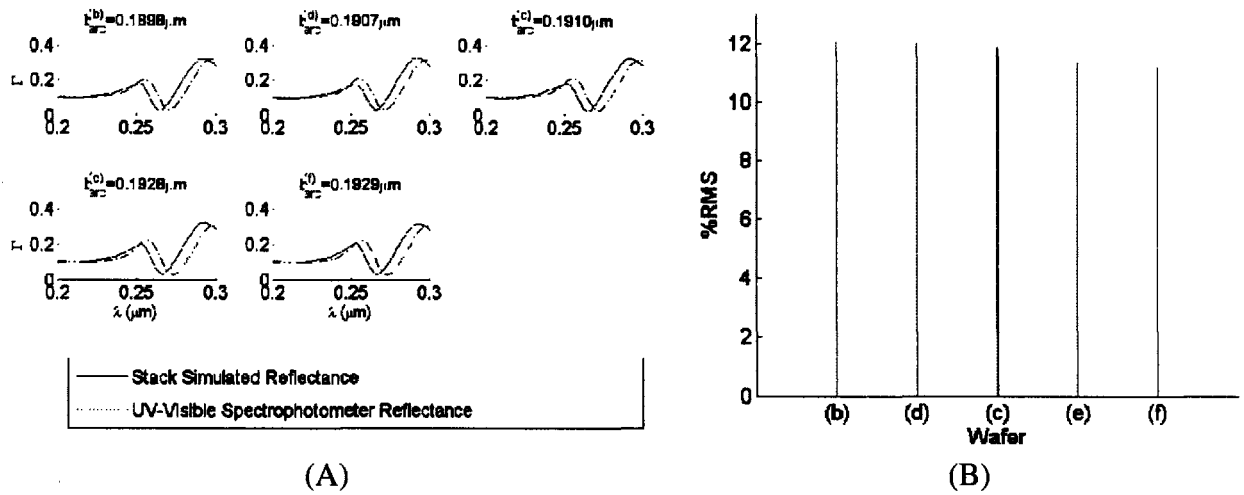


FIGURE II.2: (A) REFLECTANCE VS WAVELENGTH PLOTS FOR ARC-COATED WAFERS. (B) SHOWS RMS ERRORS BETWEEN MEASURED AND SIMULATED REFLECTANCE VS. WAVELENGTH FOR EACH ARC-COATED WAFER.

In each 'A' plot title are superscripted wafer names and the film thickness in microns.

The general agreement between single-layer measurements and simulations appear to validate our modeling and index of refraction data. The one  $\text{SiO}_2$  plot with the largest error may be due to an error in film thickness measurement.

### 3. The thickness and reflectance of evaporated SiO<sub>2</sub> coated ARC films are compared to simulated bilayer film stacks

Following the single-film comparison, bilayer stacks of SiO<sub>2</sub> evaporated on ARC were compared to verify EM-Suite's ability to accurately characterize reflections for multiple film layers.

In the following experiment, 24 wafers were coated with ARC and then SiO<sub>2</sub>. The target thickness was varied for each film, creating a 6x4 matrix of thicknesses. The matrix of bilayer stack film thicknesses is displayed as black circles (labeled with their corresponding wafer number for future reference) in Figure II.3.<sup>(4)</sup>

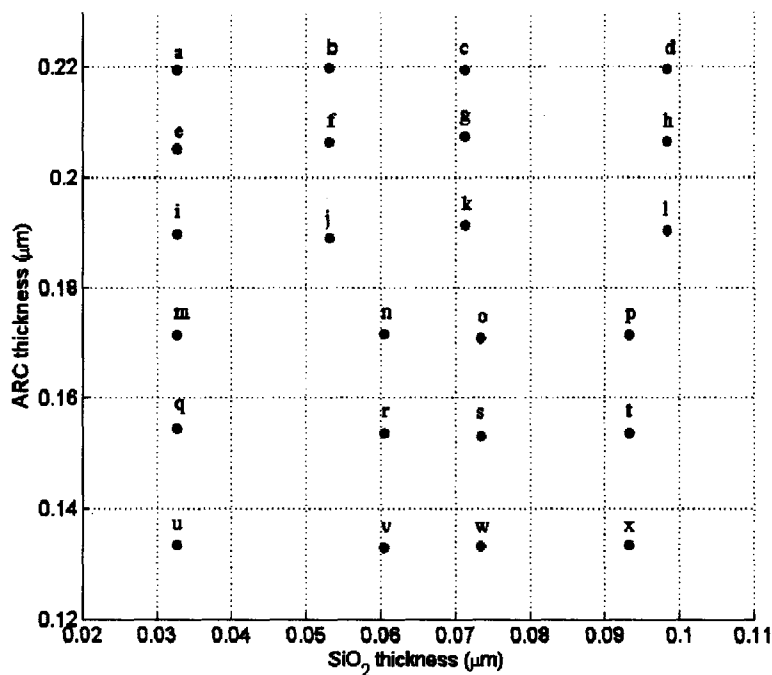


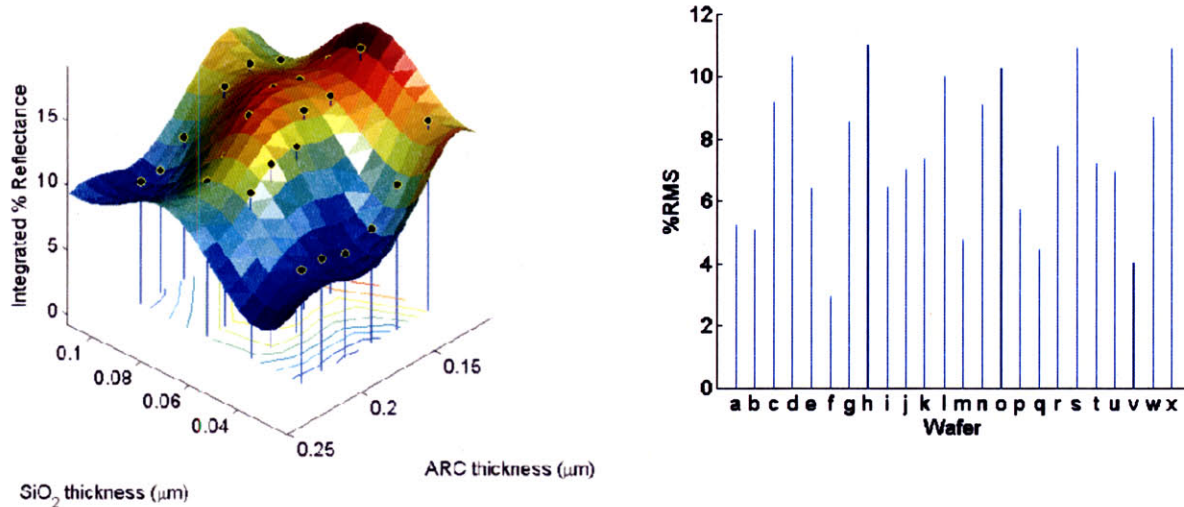
FIGURE II.3: THE 24 BILAYER STACK WAFERS ARE MAPPED BY THEIR RELATIVE FILM THICKNESSES INTO A 6X4 MATRIX OF DIFFERENT SiO<sub>2</sub> AND ARC FILMS.

Figure II.4 is a comparison of measured and simulated reflectance from the bilayer stack.

II.4.A shows the measured and simulated reflectance (integrated from 200-300 nm). The height in II.4A signifies the integrated reflectance for the circles of measured data and surface of

<sup>(4)</sup> Nonuniformity in the thickness spacing was due to run-to-run variations in SiO<sub>2</sub> coating.

simulated data. Figure II.4.B shows the RMS error between individual measured and simulated reflectance vs. wavelength curves for each of the 24 bilayer-stack-coated wafers.



(A)

(B)

FIGURE II.4: (A) INTEGRATED REFLECTANCE FOR BILAYER-STACK-COATED WAFERS. THERE ARE THREE DATA SETS OF INTEGRATED REFLECTANCE PICTURED IN THIS PLOT. THE "POLES" STICKING UP THROUGH THE SURFACE ARE THE INTEGRATED EXPERIMENTAL REFLECTANCE. THE SURFACE IS THE SIMULATED INTEGRATED REFLECTANCE OVER A WIDE RANGE OF FILM THICKNESSES, AND THE CONTOUR IS THE SIMULATED INTEGRATED REFLECTANCE OVER THE THICKNESS PAIRS FOR WAFERS A-X. (B) RMS ERROR BETWEEN SIMLUATIONS AND MEASUREMENTS OF REFLECTANCE VS. WAVELENGTH (200-300 NM) FOR 24 BILAYER STACK WAFERS. RMS ERRORS ARE ALL LESS THAN OR EQUAL TO 11%.

#### 4. The simulations predict interlayer thicknesses of the trilayer stack

With simulations and material properties confirmed by comparison to experiments, EM-Suite was used to predict the SiO<sub>2</sub> and ARC thickness that minimize the total reflectance for the trilayer stack. The same range of SiO<sub>2</sub> and ARC thicknesses for wavelengths between 200nm and 260nm was simulated on a trilayer stack having a top layer PMMA. Shown in Figure II.5 are the contours of total integrated reflectance (weighted by DUV lamp spectral intensity at the wafer and scaled by PMMA absorption) for the range of ARC and SiO<sub>2</sub> described above.

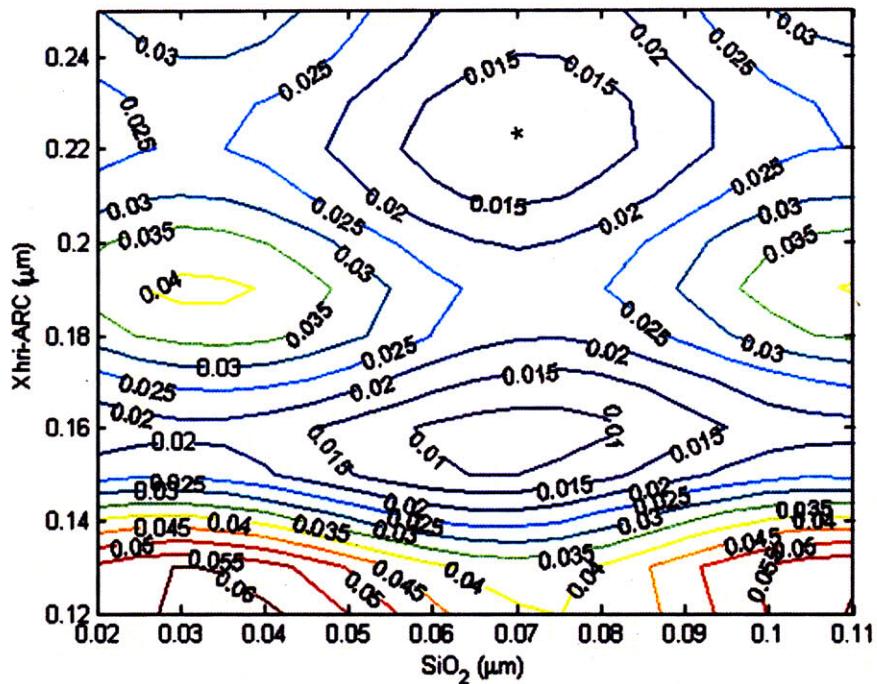


FIGURE II.5: CONTOUR PLOT OF INTEGRATED TOTAL REFLECTANCE FOR THE TRILAYER STACK ARC:SiO<sub>2</sub>:PMMA ON SILICON. THE REFLECTANCE IS INTEGRATED OVER WAVELENGTHS FROM 200NM TO 260NM FOR A RANGE OF 13 ARC AND 18 SiO<sub>2</sub> THICKNESSES. THE (\*) IS THE CHOSEN THICKNESS PAIR AT A 70NM THICK SiO<sub>2</sub> FILM AND 225NM THICK ARC FILM THAT MINIMIZES THE INTEGRATED REFLECTANCE TO UNDER 1.5% FOR UP TO 10NM VARIATIONS IN FILM THICKNESS.

The target trilayer stack thicknesses were chosen to be at the minimum of 225 nm ARC and 70 nm SiO<sub>2</sub>. This minimum allows for reasonable thickness variation ( $\pm \sim 10$  nm) while still maintaining less than 1.5% reflectance. The 1% region at thinner ARC thickness is more sensitive to changes in ARC thickness below 150nm and consequentially was not chosen.

The benefit of simulating exposures using a trilayer stack with the appropriate film thicknesses will become evident in the next chapter. However, it is sufficient to note that the single-layer PMMA stack is an extreme case of a trilayer stack. So, examining Figure II.4 again, a vanishing SiO<sub>2</sub> and ARC thickness tends to increase the reflectance, causing more (undesirable) interference.

### III. Intensity Simulations

This chapter will present simulations performed using finite-difference time-domain (FDTD) Maxwell's-equation numerical-simulation software. EM-Suite, from Panoramic Technologies, was used to simulate CCL exposures. The latter part of this chapter will present intensity profiles within the PMMA resist during exposure and discuss how linewidth measurements (assuming a resist clipping model of development) are extracted from these intensity profiles.

By their nature, numerical simulations have discrete variables [30]. Finite-difference simulations perfectly mimic analytical models only in the limit where the discretization becomes continuous. While attractive in principle, an infinite number of values take impractically long to simulate. The first sections of this chapter will describe how a simulation is set up in E-M Suite and discuss the optimization of the discretization of a number of variables within the simulation (two-dimensional space, the Xe-Hg lamp power spectrum, angle of illumination, etc.) The method used is to vary the discretization, or number of values, of each of these variables from a very high number (more closely mimicking reality) to a lower, more practical value. The RMS error between the “perfect” and progressively less perfect simulations is used to choose the discretizations that balance accuracy and efficiency.

#### 1. E-M Suite Optimizations

Within E-M Suite, an *environment* is defined by variables and their values. The environment then specifies the spatial geometry and wave source as well as initializes the material configurations using uploaded index-of-refraction models. The spatial geometry, or total volume of composed cells, is controlled by its smallest length scale, or cell size. The diffuse wave source (see Figure I.3) simulated within E-M Suite includes both TE and TM polarizations

with associated amplitudes and phase. In addition to choosing the appropriate cell size, Pistor suggests that placing the wave source a few cells from the top of the simulation space can also reduce FDTD errors [30]. Figure III.1 is an example of a simulated CCL environment. It depicts a 300 nm pitched grating of 2:1 duty cycle (chrome lines:spaces) with a trilayer stack on a silicon wafer exposed with a standard chrome mask (SCM).

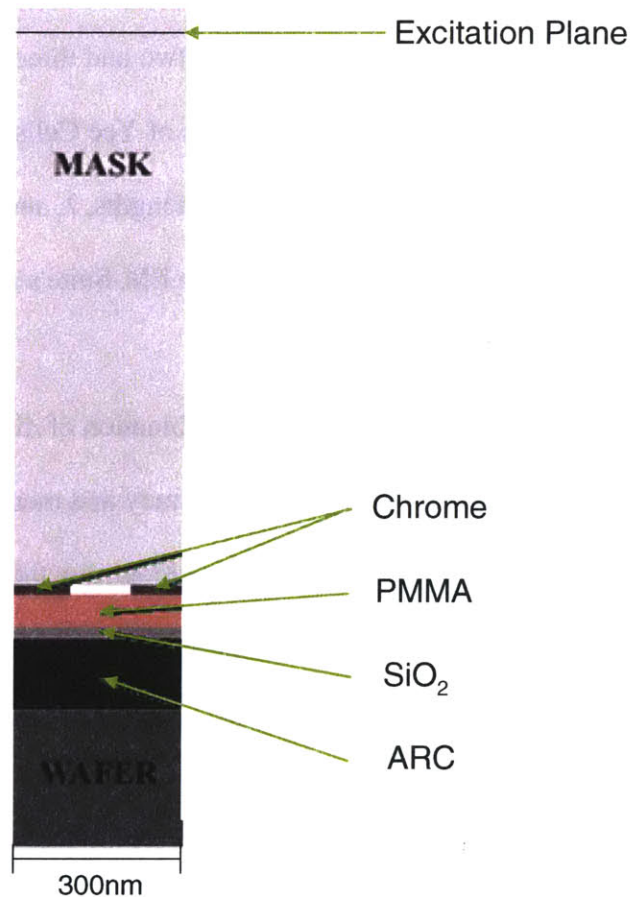


FIGURE III.1: THE CCL TRILAYER STACK SIMULATION SPACE FOR A 100NM LINEWIDTH. WITHIN THE SIMULATION ENVIRONMENT, LIGHT IS INITIATED AT THE EXCITATION PLANE AND PROPAGATES THROUGH THE FUSED SILICA MASK- SEE FIGURE I.3, INTO THE ABSORBER LAYER OF CHROME LINES (IN THIS CASE 100NM LINES:SPACES AT A 1:2 DUTY CYCLE). A VACUUM (STANDARD MASK) OR FUSED SILICA (EMBEDDED AMPLITUDE MASK) LIES BETWEEN THE CHROME ABSORBER LINES. LIGHT PROPAGATING PAST THE ABSORBER LAYER IRRADIATES THE PMMA DUV RESIST, AND REFLECTS OFF OF A LAYER OF SILICON DIOXIDE AND ANTI-REFLECTION COATING (ARC) AND A SILICON SUBSTRATE.

a. Memory Requirements and Running time

FDTD simulations use volumes of space, called Yee-cells, to solve Maxwell's equations iteratively for alternating cube vertices<sup>(5)</sup> [30]. EM-Suite electromagnetic wave simulations require populating variables with their respective values. The environment, or populated variables, constrains Maxwell's equations. Configured to be spatially periodic in the x- and y-direction, EM-Suite simulates repeated "dense" features in two and three-dimensional form. In the first part of this chapter, the separation between vertices of Yee Cells,  $\delta_i$ , the discretized Xe-Hg diffuse electric field amplitudes,  $E_j(\lambda_j)$ , associated wavelengths,  $\lambda_j$  and angular spread,  $\theta_k$  are optimized. Establishing optimal  $\delta_i$ ,  $E_j(\lambda_j)$ ,  $\lambda_j$  and  $\theta_k$  increase EM-Suite's modeling fidelity without sacrificing simulation speed.

EM-Suite solves Maxwell's equations for each combination of discrete variable values. Therefore, each variable's values constrain EM-Suite's accuracy and memory usage: having a continuous variable (with an infinite number of values) would burden the simulator memory, while having a single discrete value would lead to inaccurate simulations. Similarly, the simulation runtime depends on the number of variable values and variables assigned in the simulation environment.

The simulation memory and runtime are characterized in terms of the total volume of space ( $\Delta x \Delta y \Delta z$ ) being simulated to the partial volume of a cell ( $\delta_x \delta_y \delta_z$ ), [31]:

$$\begin{aligned} \text{Memory:} \quad M &\propto \frac{\Delta x \Delta y \Delta z}{\delta_x \delta_y \delta_z} \\ \text{Simulation Runtime:} \quad T &\propto \frac{\Delta x \Delta y \Delta z}{\delta_x \delta_y \delta_z} \frac{\Delta z}{\Delta t} \end{aligned}$$

---

<sup>5</sup> Technically, the discrete field equations skip a Yee-cell in evaluation so that the numerical difference described here is actually the distance between every two Yee-cells. [30]



Comparing the simulations to experiments with exposed gratings (a two-dimensional geometry) did not require running any three-dimensional simulations. From the memory and runtime equations it is clear that two-dimensional simulations had the additional benefit of saving time because the ratio of  $\Delta y$  to  $\delta_y$  becomes 1.

#### b. EM-Suite Environment

The fidelity of the numerically-simulated intensity profiles is optimized here for physically inspired variables. Because EM-Suite simulations repeatedly solve Maxwell's equations for each set of variable values within the environment, assigning too many values to the environment's variables results in inefficient simulations. However, determining the optimal variable resolution, or number of values, creates well-defined simulations that are able to run efficiently and effectively.

Of course, the optimal case and all others must be gauged relative to some numerically-determined best case. Contributing two degrees of freedom, the cell size,  $\delta_i$ , is the most important parameter to optimize. To determine the optimal cell size,  $\delta^*$ , a numerical experiment was run simulating exposure of a 1  $\mu\text{m}$  line:space feature on the trilayer stack on silicon. In these experiments, the cell size was varied from 4 nm to 40 nm in 4 nm steps. Conceptually, this is the same as choosing the number of cells per wavelength [30].

The resulting 2-dimensional intensity profiles, each a different size matrix of intensity values, were compared. The best-case cell-size, having the most variable values, resulted in the longest run time. Differences in the size of the matrices required additional processing – the best case was resampled into an appropriately sized, comparable image. By resampling the best-case profile it was possible to generate the RMS error between the best-case and more efficient cases.

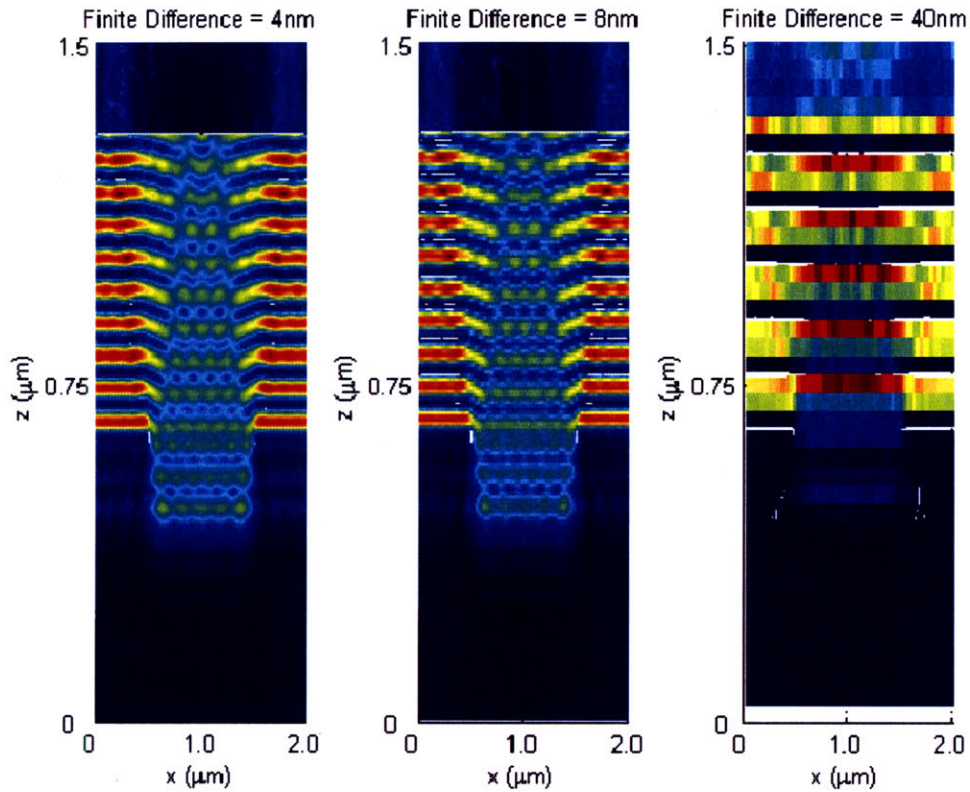


FIGURE III.2: THE BEST, NOMINAL AND WORST INTENSITY PROFILES FOR VARIATIONS TO THE YEE-CELL SIZE. NOTE PISTOR'S RECOMMENDED OPTIMAL YEE-CELL SIZE, OR FINITE DIFFERENCE, IS NEAREST TO 8NM. THE DIFFERENCE IN THE SIMULATED INTENSITY DOES NOT APPEAR TO BE SIGNIFICANTLY DIFFERENT FOR 4 NM AND 8 NM CELL SIZES, BUT THE SIMULATION DEGRADES SIGNIFICANTLY FOR THE LARGEST (40 NM) CELL SIZE.

Figure III.2 shows three simulated cases (4 nm, 8 nm, and 40 nm cell size) of the numerical cell-size experiment. Clearly the cell size of 40nm is too large to provide useful simulations, while the 8 nm cell size (closest to Pistor's recommendations) appears to be visually similar to the highest-resolution simulation.

In addition to choosing the cell-size, choosing the proper number of wavelengths to represent the lamp spectrum was important both for simulation accuracy and efficiency: the broad spectrum of the Xe-Hg lamp prohibits simulating at a single wavelength. Wavelength values,  $\lambda_j$ , were bounded between 200nm to 260nm and varied in number of values,  $j$ , from 30 to

20, 10, 9, 8, 7, 6, 5, 4, 3 and 2, making the discretization, ( $\lambda_j=60\text{nm}/j$ ), vary from 2 nm to 30 nm wavelength steps.

Bounding the range of angles of light exiting the collimating lens is specified to be within  $\pm 2^\circ$  of normal incidence. The simulated discrete collimating angle,  $\theta_k$ , was also specified over this range but was varied in discretization,  $k$ , from 21 to 19, 17, 15, 13, 11, 9, 7, 5, 3 and 1 angle values.

RMS comparisons were obtained for the discretized power spectrum and angular spread by again comparing the *best* profile to others of decreasing variable resolution. Optimizing these variables was simpler than optimizing the cell-size because the simulation outputs were the same size.

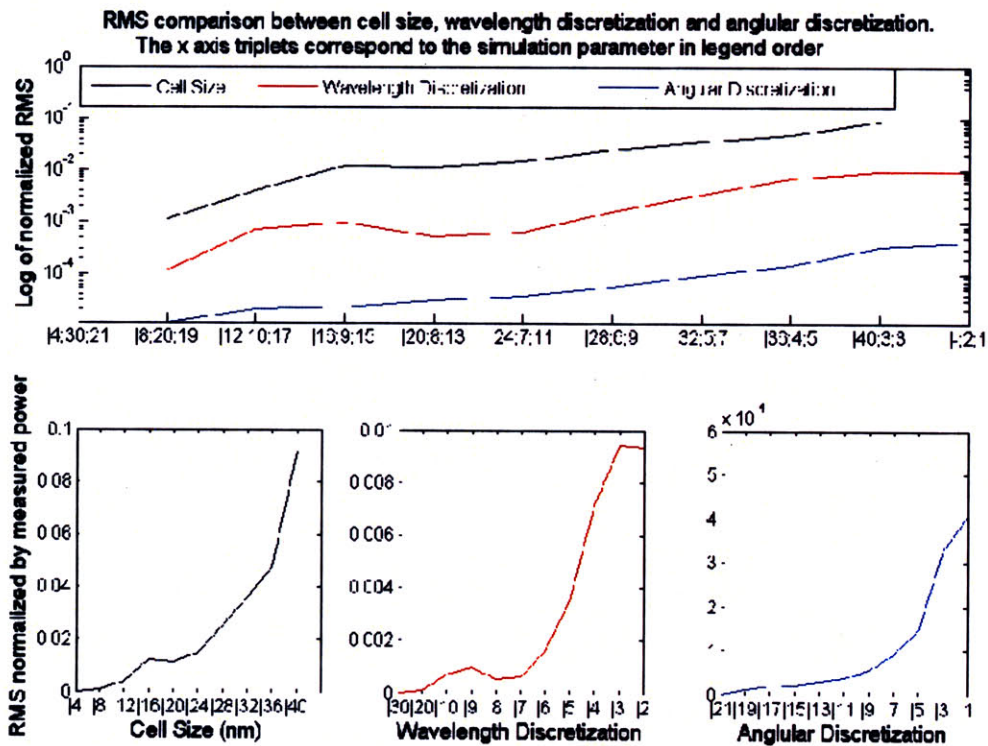


FIGURE III.3: THE ROOT-MEAN-SQUARE ERROR BETWEEN THE BEST CASE AND OTHER CASES OF CELL SIZE ( $\delta^*$ ), WAVELENGTH DISCRETIZATION ( $\lambda^*$ ), AND ANGULAR DISCRETIZATION ( $\theta^*$ ). THE TOP GRAPH SUGGESTS THAT THE SIMULATIONS ARE MOST SENSITIVE TO CHANGES IN CELL SIZE. NEXT ARE CHANGES IN THE NUMBER OF DISCRETE POWER SPECTRA. FINALLY, CHANGES IN ANGLE AFFECT THE SIMULATION QUALITY LEAST.

Figure III.3 shows the RMS errors for all three numerical optimizations. The bottom row of plots shows individual RMS errors (normalized to average intensity) from best-case simulations as the discretization is decreased for LEFT: cell size, CENTER: wavelength, and RIGHT: Angle. All three show a range of discretizations with relatively small error, then rapid increases in RMS error as discretization decreases.

The top plot shows the three errors plotted simultaneously. This plot clearly shows that the cell size error dominates the other errors, indicating that small cell size is the most important discretization to maintain when balancing simulation accuracy with run time. Note that as the Yee-cell size increases past 12nm it causes worse RMS errors than obtained for the worst values of the optimized variables. In Table III.a are the optimal parameters used in the simulations for this thesis.

Symbol	Variable	Value
$t_{ox}$ (nm)	SiO <sub>2</sub> Thickness	70
$t_{arc}$ (nm)	ARC Thickness	225
$\delta$ (nm)	Cell Size	10
$\lambda$ (nm)	Wavelength	[205, 218, 230, 242, 255]
E (mV/cm)	Field Amplitude	[ $6.3 \times 10^{-3}$ , $18 \times 10^{-3}$ , $70.9 \times 10^{-3}$ , $108.9 \times 10^{-3}$ , $72.1 \times 10^{-3}$ ]
$\theta$ (°)	Collimating Angle	[-2, 0, 2]

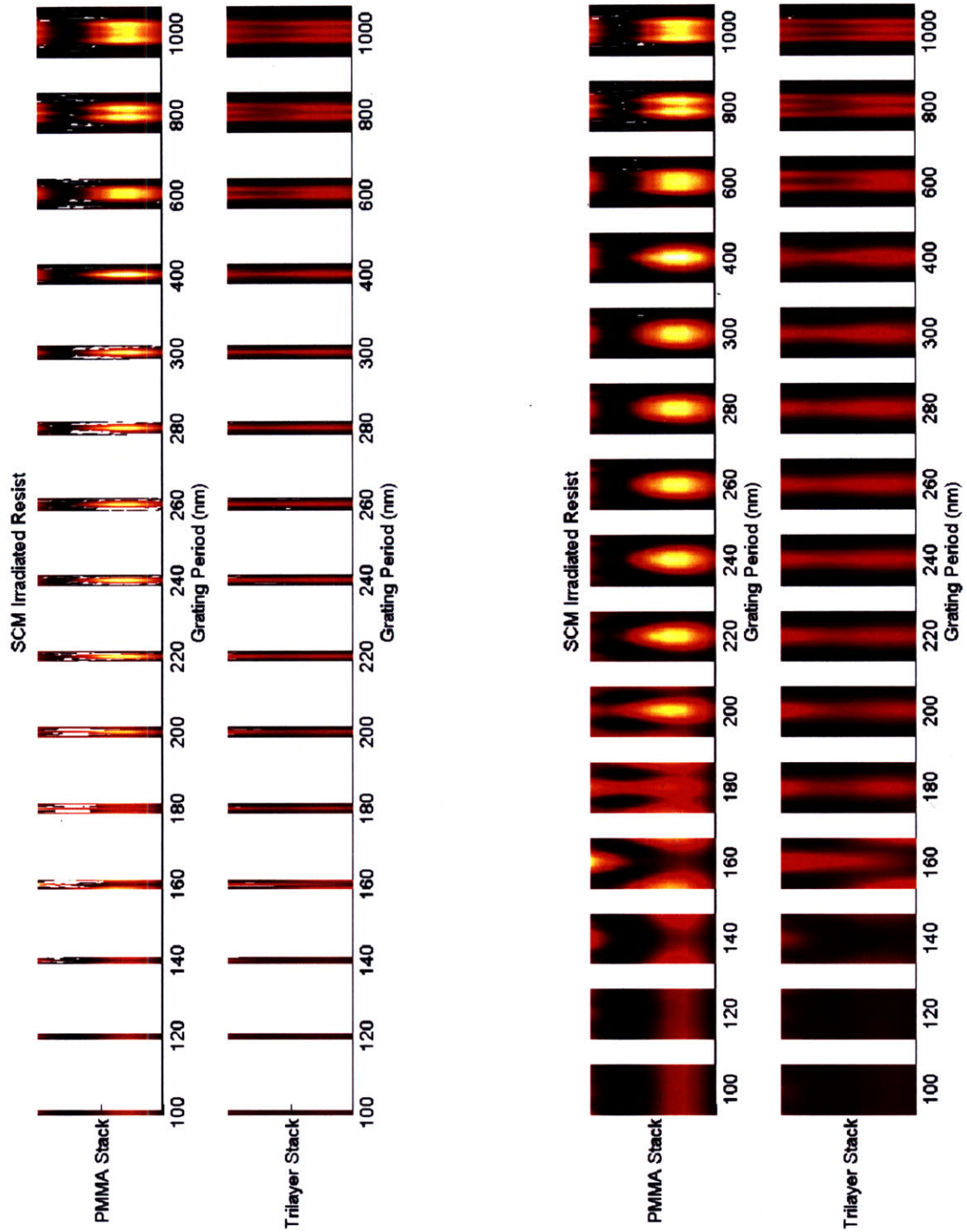
TABLE III.a: THE SIMULATION ENVIRONMENT. THE VALUES IN THIS TABLE WERE FOUND THROUGH THE OPTIMIZATIONS DETAILED IN CHAPTER 2 AND THE PRESENT CHAPTER THE SUM OF THE SQAURED FIELD AMPLITUDES WAS NORMALIZED TO THE AVERAGE MEASURED LAMP INTENSITY, 22.4 mW/cm<sup>2</sup>. THE FIELD AMPLITUDES WERE CHOSEN AT THE DISCRETE WAVELENGTHS BY FIRST SEGMENTING THE DUV SPECTRUM AND THEN AVERAGING THE INTENSITY FOR EACH SEGMENT.<sup>6</sup>

Our cell size optimization agrees with published FDTD recommendations: according to Pistor [29, 30] a cell size of one-fifteenth the wavelength in the highest-index material gives a 2% error. The highest index of refraction occurs in the PMMA resist: at 200nm (the lowest wavelength from the source) the real index of refraction is 1.61. Thus, a 2% error should result from an optimal cell-size of  $\delta^* \sim 9\text{nm}$ .

<sup>6</sup> EM-Suite required post simulation processing, during which the simulated intensities for each simulated wavelength were scaled by the PMMA absorption.

## 2. EM-Suite Simulations

Having established the simulation environment, intensity profiles in the resist were simulated for exposures of dense (1:1) line:space features. Shown in Figure III.4 (next page) are simulated intensity profiles within the PMMA resist of both a single-layer of PMMA and trilayer stack. Two versions of the simulations are shown: the images in (A) are to scale in the x-dimension and the 90nm PMMA thickness is of the same scale for each plot. In this case, details of the finer-linewidth simulations are difficult to see. In III.4b, the same simulations are shown, but the x-axis is normalized for clarity.



(A) (B)

FIGURE III.4: THE SIMULATED RESIST INTENSITY PROFILES OF THE IRRADIATED SINGLE LAYER OF PMMA (TOP ROW) AND TRILAYER (BOTTOM ROW) STACKS USING THE STANDARD MASK. IN (A) THE X-AXIS SCALE IS MAINTAINED TO REPRESENT THE TARGETED PITCH OF EACH GRATING. IN (B) THE X-AXIS IS NORMALIZED BY THE PITCH TO CLARIFY THE INTENSITY PROFILES OF THE SMALLER FEATURES.

It is clear that the minimization of reflectance from the trilayer stack has several benefits. The intensity profile through the resist (in  $z$ ) is more uniform, and a uniform linewidth (in  $x$ ) persists to perhaps 220 nm or 200 nm period for PMMA only, and to 180 nm period or below for the trilayer stack configuration.

In addition to the simulation of a single-layer PMMA and trilayer stack, exposures using the EAM and SCM masks were simulated for the trilayer stack (Figure III.5).<sup>7</sup>

---

<sup>7</sup> The bottom row in III.4 and top row of III.5 are identical, though the intensity scale is not preserved between III.4 and III.5.

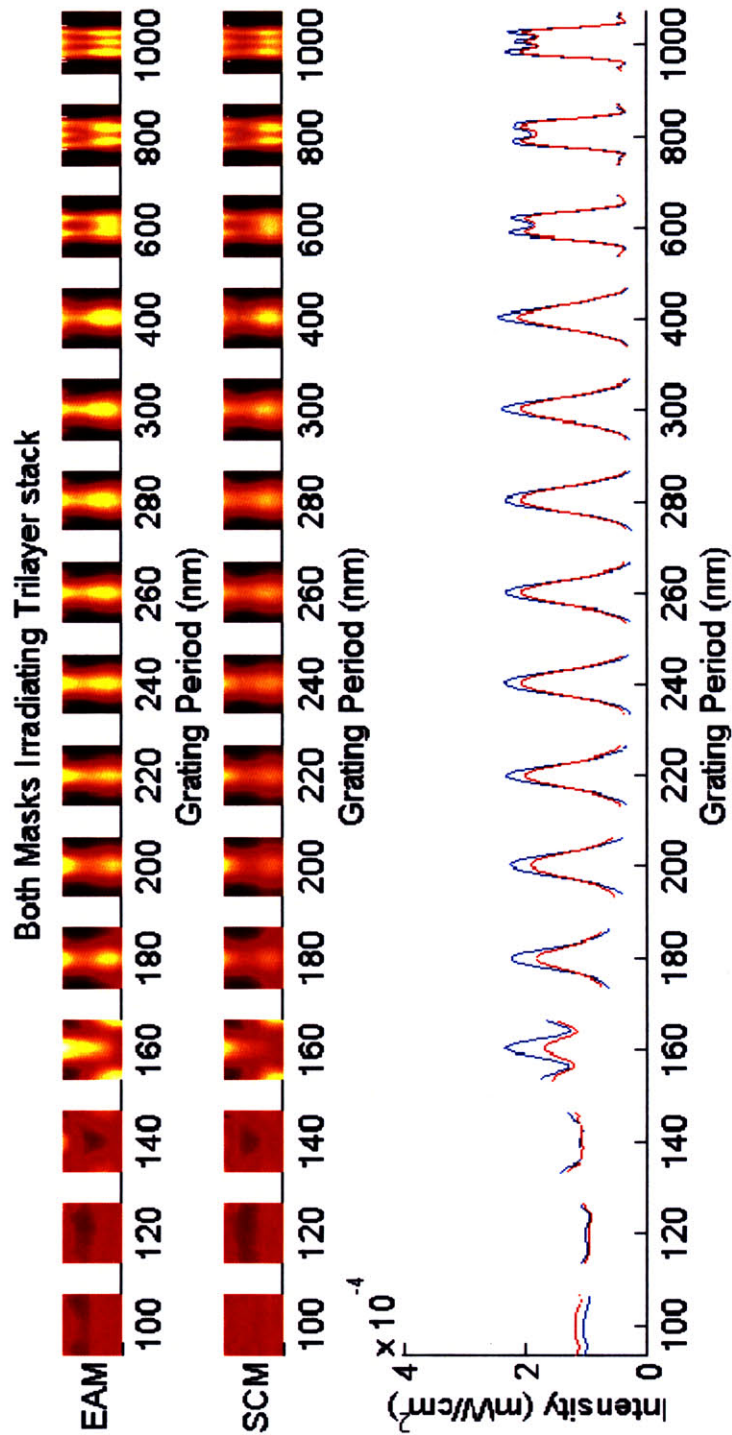


FIGURE III.5: TOP AND CENTER: SIMULATED INTENSITY PROFILES WITHIN THE PMMA RESIST FOR EAM AND SCM FOR DIFFERENT LINWIDTHS. THE INTENSITY SCALE IS MAINTAINED BETWEEN ALL PROFILES. BOTTOM: INTENSITY PROFILE (AVERAGED IN Z) FOR EAM (BLUE) AND SCM (RED). NOTE CAREFULLY THE DIFFERENCE IN THE PROFILES BETWEEN EACH MASK TYPE: INTENSITY IS HIGHER IN THE RESIST FOR EAM, AND AS THE PITCH DECREASES THE CONTRAST IS MAINTAINED TO SMALLER LINWIDTHS FOR THE EAM.



In III.5, the EAM-exposed PMMA is penetrated by light more easily than with the SCM. Comparing the profiles for each mask, the steeper sidewall slope (especially noticeable below grating periods of 220nm) and higher contrast of the EAM simulations suggest a more uniform pattern transfer.

a. Simulated Linewidth Measurements

This section will show the process of extracting linewidth vs. dose from a simulated intensity profile (in this case a 300nm-pitch grating exposed in PMMA resist on a trilayer stack). Figure III.6 details the process of finding the intensity value which yields a desired linewidth.

Figure III.6A shows the raw simulated intensity profile from EM-Suite with the mask linewidth indicated by blue dashed lines. Linewidth measurements were taken from the simulations by measuring the distance between contour lines of a given intensity. Figure III.6B shows the same profile with a contour drawn at the intensity value which yields the mask linewidth (150 nm) halfway up the resist. III.6.C shows a contour that was chosen to give the mask linewidth over an average of five points over the middle 40% of the PMMA resist.

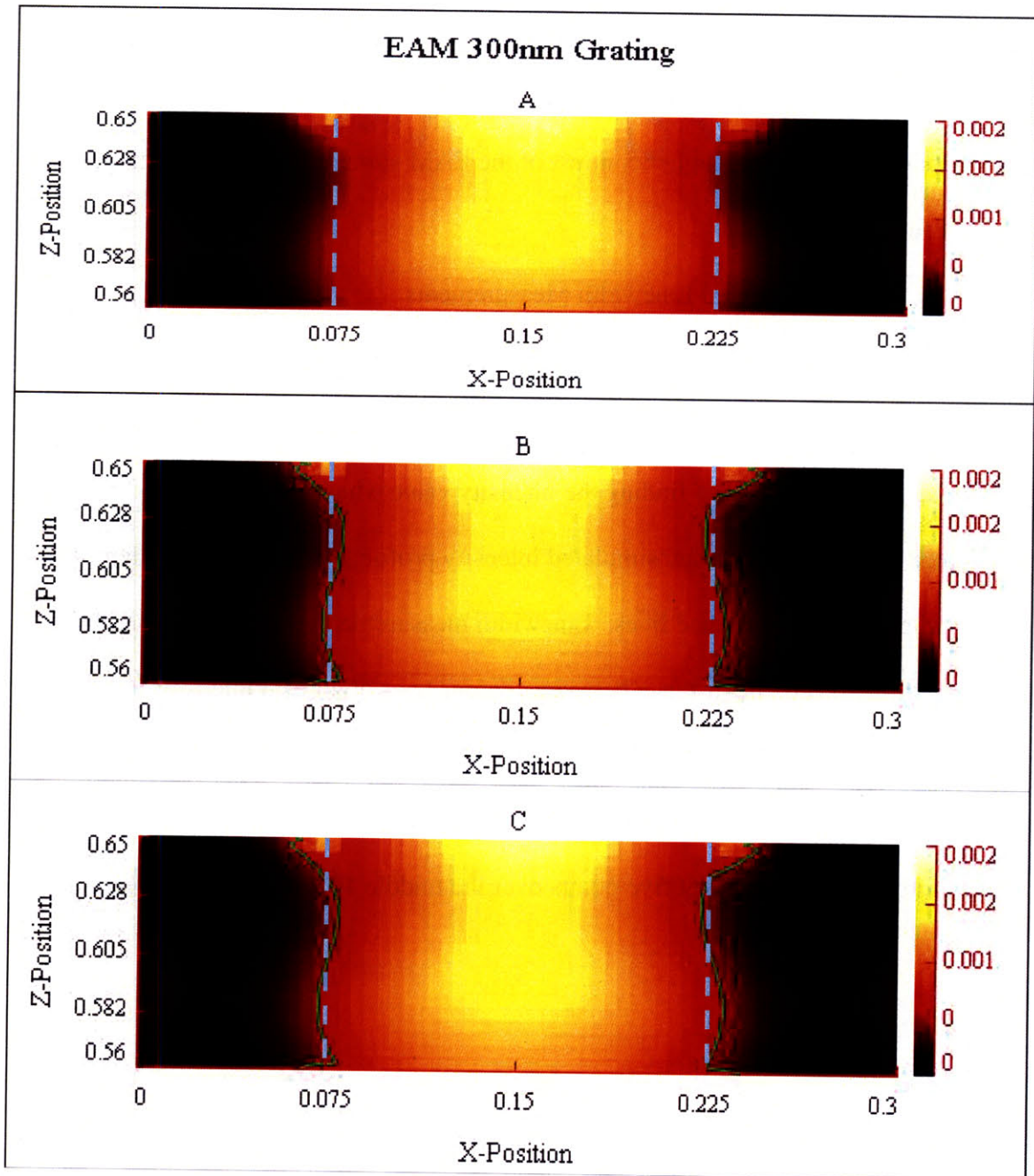


FIGURE III.6: SIMULATED INTENSITY IN THE PMMA OF A 300NM-PITCH TRILAYER-STACK EXPOSURE USING THE EAM. (A) SHOWS THE SIMULATED INTENSITY PROFILE IN PMMA (MASK LINewidth INDICATED BY BLUE DASHED LINES). (B) DEPICTS THE CONTOUR THAT INTERSECTS THE MASK LINewidth (150 NM) HALFWAY UP THE RESIST ( $Z = 605\text{NM}$ ). (C) DEPICTS THE NOMINAL CONTOUR CORRESPONDING TO THE AVERAGED INTENSITY AT THE MASK LINewidth AS  $Z$  RANGES FROM  $587\text{NM}$  TO  $623\text{NM}$ . NOTICE THE SLIGHT DIFFERENCE BETWEEN THE CONTOUR IN (B) AND (C). THE ASYMMETRY OF THE CONTOURS IS A NUMERICAL ARTIFACT FROM EM-SUITE. THE COLORBAR SCALING IS AN ARTIFACT OF THE SIMULATION SOFTWARE.

For the simulated linewidth measurements presented in this thesis, the average contour at mask linewidth was used as a starting point (III.6C). The intensity was then varied in 10%

increments, up to +400%/-100% to generate additional contours. Linewidths were measured halfway up the resist.

Shown in III.7 is the simulation from III.6 with contours drawn at the intensities: nominal - 50%, nominal and nominal + 50%.

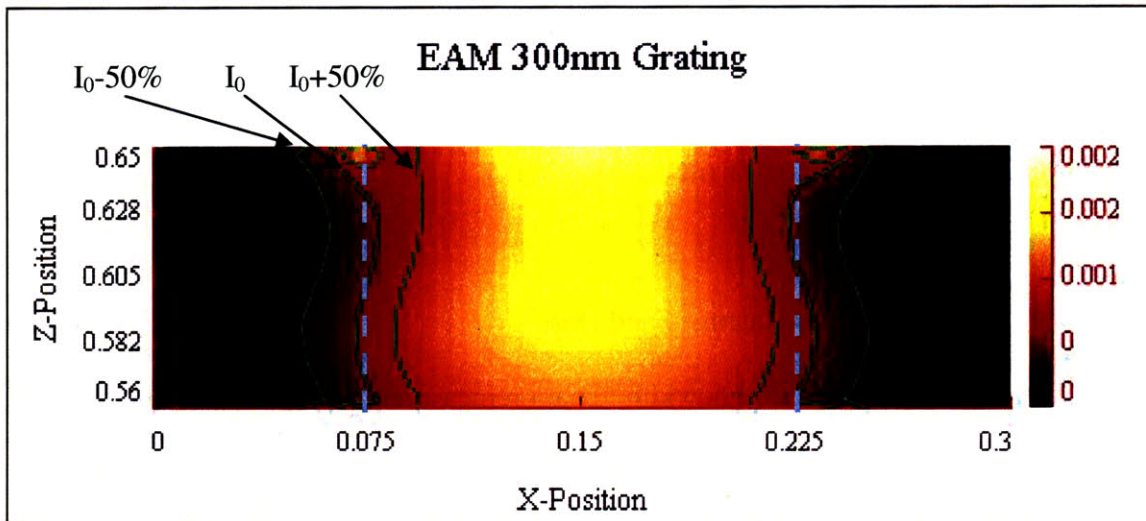


FIGURE III.7: CONTOURS ARE DRAWN ON THE 300NM PERIOD GRATING FOR THE NOMINAL INTENSITY AND  $\pm 50\%$ .

#### b. Linewidth measurement limitations

Linewidth measurements performed as shown above do not always result in smooth linewidth vs. dose curves. A simulated 300nm period (trilayer) resist for the EAM and SCM are shown in Figure III.8 with contours drawn at the nominal intensity, and 80%, 60%, 50% and 40% of the nominal intensity.

The outermost, 50% and 40%, contours in III.8A show that, with a clipping model of development, the resist would collapse and not faithfully replicate the feature. This is likely due to constructive interference of the diffracted light from adjacent apertures.

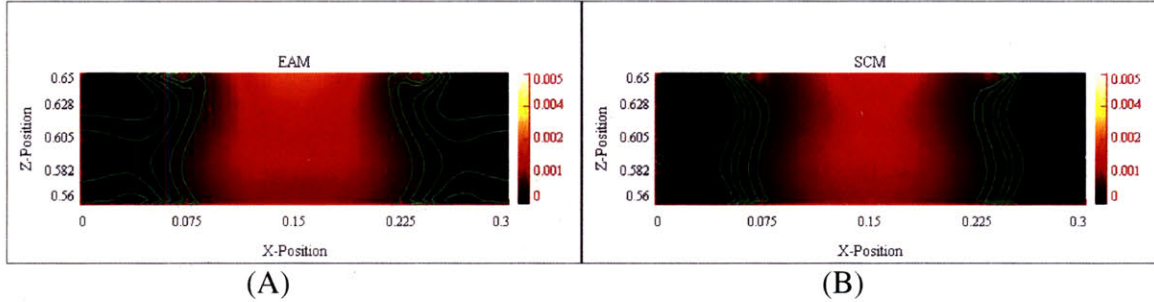


FIGURE III.8: SIMULATED INTENSITY WITHIN THE PMMA RESIST ABOVE THE TRILAYER STACK. THE CONTOURS IN EACH IMAGE, MOVING OUTWARD FROM THE CENTER OF THE RESIST, BEGIN AT THE INTENSITY CORRESPONDING TO THE TARGET LINewidth THROUGH THE CENTER OF THE RESIST. THE REMAINING CONTOURS ARE AT 80%, 60%, 50% AND 40% OF THE NOMINAL INTENSITY. IN A, THE 50% AND 60% CONTOURS PENETRATE THE RESIST HORIZONTALLY CAPPING THE MEASURED LINewidth (FROM THE CENTER OF THE RESIST) THAT EXTENDS BEYOND THE SIMULATION SPACE TO 300NM. THE SAME IS NOT TRUE OF THE CONTOURS IN B.

### c. Linewidth vs. Intensity and Dose

In Figure III.9A are plotted linewidth variation measurements. In III.9B, the same variations are transformed from intensity variations to dose variations. This is detailed below.

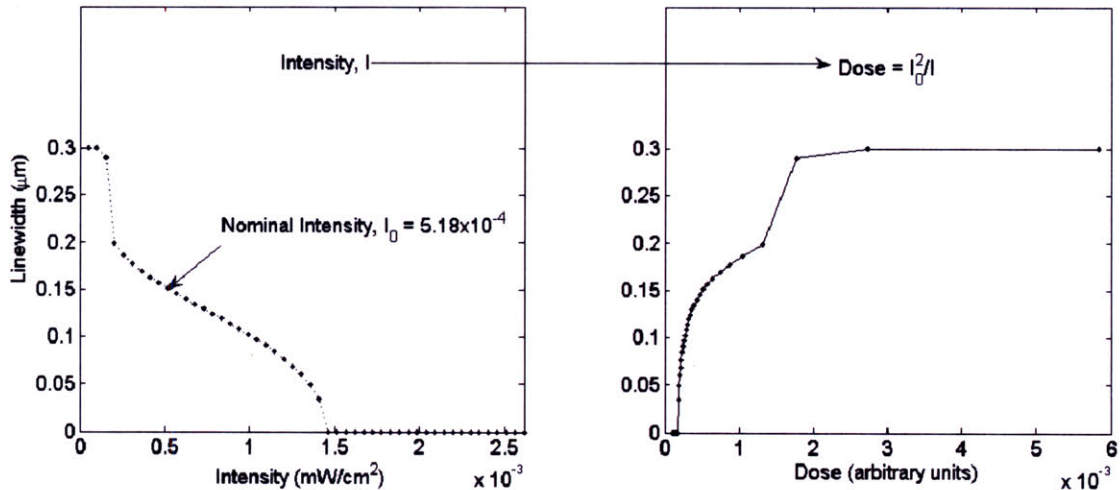


FIGURE III.9: (A) LINewidth vs. INTENSITY LEVEL FOR THE SIMULATED 300 NM PERIOD EXPOSURE SHOWN PREVIOUSLY IN III.7 & III.8A. THE NOMINAL INTENSITY,  $I_0$  GIVES A LINewidth CLOSEST TO THE MASK LINewidth. AS EXPECTED, THE LINewidth DECREASES WITH INCREASING INTENSITY. THE DATA IN (A) IS TRANSFORMED INTO LINewidth vs. DOSE IN (B) BY ASSUMING A CLIPPING MODEL FOR DEVELOPMENT WHERE INTENSITIES GREATER THAN THE NOMINAL INTENSITY DEVELOP OUT COMPLETELY. FURTHERMORE, THE INTENSITY VARIATIONS ARE TRANSFORMED INTO DOSE (SEE TEXT).

With a clipping model of resist development, we assume the resist develops out completely for all intensities larger than a given intensity,  $I_0$ . If the exposure time (and therefore dose) were doubled, then the intensity level whose profile gives the same linewidth would be halved from its original value. This inverse relationship between contour intensity,  $I$ , and effective dose,  $D_{\text{eff}}$ , required transforming the intensity variations as follows:

$$D_{\text{eff}} = (1/I)I_0D_0$$

Where  $D_0=I_0t_0$  is the nominal dose<sup>(8)</sup> required to achieve the mask linewidth.

The term  $1/I$  results from the inverse relationship described above. The remaining terms in the equation serve to properly normalize the dose. At  $I = I_0$ , the effective dose equals  $D_0$ . Halving the intensity level at which the contour is taken to  $I=I_0/2$ , should (and does) yield an effective dose of  $2D_0$ .

The effective dose transforms the data shown in Figure III.9A into the data shown in III.9B. Chapter V will compare these transformed simulated linewidth vs. dose measurements with experimental measurements, which are presented in the following chapter.

---

<sup>8</sup> Our scaling of the incident spectrum with resist absorption (which is in units of inverse  $\mu\text{m}$ ) means that we are not using an accurate dose in our clipping model. However the scaling of our intensity-to-dose transformation allows accurate comparisons between simulations, maintaining differences in intensity in the resist shown in Figure III.5.

#### IV. Linewidth vs Dose

As PMMA is exposed to DUV light it is chemically modified. Over the DUV range (200nm to 260nm) the PMMA's imaginary index of refraction is relatively large up to 240nm (see Figure I.5). Correspondingly, within the PMMA, the photons cause chain scissioned ester bonds [5]. As a consequence, the dose of photonic energy exposing the resist is related to the amount of resist removed during development.

The minimum resolvable feature of an exposure system, like the CCL system here, plays an important role in design. In searching the literature, a widely-used equation predicting the smallest resolvable feature in contact lithography was tracked back to D. Widmann [32], 1976 <sup>(9)</sup>. The equation relates the linewidth,  $L$ , of a periodic grating exposed at a wavelength,  $\lambda$ , to the gap separating the mask and wafer and the thickness of the imaging layer of resist,  $d$ :

$$L = \frac{3}{2} \sqrt{\lambda \left( \text{gap} + \frac{1}{2} d \right)}$$

For CCL exposures, assuming  $\lambda=230\text{nm}$  and no gap, the Widmann Limit becomes 160nm for a resist 100nm thick. One limitation of the Widmann equation is its failure to account for the resist's index of refraction.

More recently than D. Widmann *et al.*, M. Paulus *et al.* [21] presented a simulation study of both gold and chrome absorbing lines in three masks: a SCM and EAM in addition to a modified EAM. The modified EAM used embedded chrome lines that were thinner than the surrounding fused silica mask. For contact lithography, they reported that the resolution limit was:

$$L = \frac{\lambda}{2n}$$

---

<sup>(9)</sup> Widmann's references were read but no further information on the assumptions behind this equation were found.

Where  $n$  is the index of refraction in the gap between the absorbers (1 for our SCM and 1.61 for our EAM). Following Paulus, the suggested resolution limit is 71.5nm for a 230nm wavelength source with an EAM mask (maximum index 1.61), or 115 nm for an SCM mask. In contrast to the Widmann equation, the Paulus equation fails to account for resist thickness and incorporates the material index of refraction.

Paulus *et al.* also predicted that an EAM mask should show a higher intensity in the resist than an SCM, due to the two extra reflective interfaces (glass-air and air-resist) present in the opening of the SCM. We saw similar differences in intensity for SCM and EAM masks in our simulations (Figure III.5).

It should be noted that neither of these papers analyzed a trilayer stack configuration. It appears that Paulus assumed no wafer (only resist beyond the mask), and analyzed intensity profiles 10 nm below the mask. In real exposures, the presence of a potentially reflective surface below the resist and a resist layer of more than 10 nm thickness would certainly have an impact upon the resolution limit.

Experimentally, a 140nm period with 70nm linewidth was printed by Alkaisi *et al.* using 365-600nm ultraviolet radiation masked by a metal grating pattern on a 2 $\mu$ m-thick Si<sub>x</sub>N<sub>y</sub> membrane (supported by an outer silicon ring). In their approach, diffracted evanescent modes expose a trilayer stack (tailored to their exposure spectrum). Using evanescent modes, they are able to resolve 70nm lines on a 140nm grating, which is approximately one-sixth their peak exposure wavelength of 436nm. To explain this, they simulate resist intensity profiles and find a linear relationship between the resist's depth of field (DOF) and grating pitch, where the DOF is defined as the depth into the resist with sufficient contrast to resolve gratings of known pitch. Through a simulation study, they suggest that the smallest resolvable feature using their process

is 20nm assuming that 10nm of resist can sufficiently mask the substrate [33]. The effect of changing the resist thickness for DUV CCL was explored and is presented in the appendix.

### **1. Experiment: expose wafers at different doses using both masks**

Wafers were coated by Draper staff with 80nm of SiO<sub>2</sub> and 230nm of ARC restricting the trilayer stack to a reflectance less than 1.5% (Figure II.5) and exposed in the CCL aligner over doses between 3200 mJ/cm<sup>2</sup> and 9000 mJ/cm<sup>2</sup>. Exposed wafers were developed in 1:2 MIBK:IPA for 60s at 20°C ± 1°C, then were rinsed in IPA for 60s and finally were coated with gold-palladium for SEM imaging. The SEM images were characterized in line-width,  $\mathcal{L}$ , and standard deviation,  $\sigma$ , across the majority of patterned features for both masks.

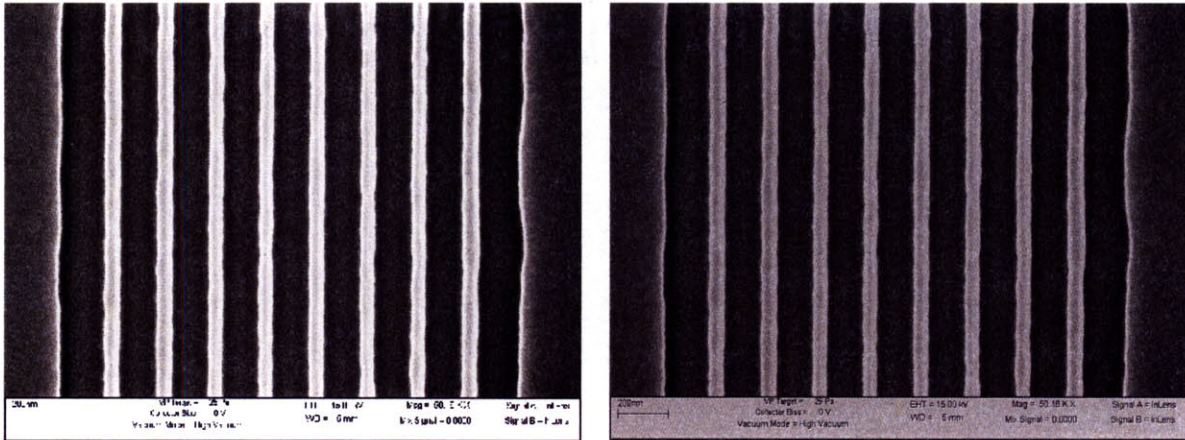
Two groups of wafers were exposed. The first group was exposed using the EAM mask and the second group was exposed using the SCM mask. Each group of wafers underwent the same development and rinsing procedures but within each group the dose was varied. For the EAM, the wafers were exposed over the range from 3200 to 8400 mJ/cm<sup>2</sup>. Similarly, for the SCM, the wafers were exposed over the range from 5400 to 9000 mJ/cm<sup>2</sup>. These dose ranges were chosen based upon optical microscope inspection of the patterns at the time of development, attempting to bracket an optimal dose.

Each exposed wafer was imaged by Draper staff using an SEM. There were 10 wafers exposed using the EAM and 7 exposed using the SCM. Forty-five images were taken per wafer (five grating periods, three duty cycles/period, and three patterns on the wafer).

To calibrate the image scale, the number of pixels per nm was calculated from the SEM scale bar. Then, the picture intensity was equalized and transformed using a filtering routine provided in the image analysis software, yielding the following (note the difference between



IV.1A and IV.1B). Use of the filtering routine greatly improved automated linewidth measurement yield without significantly altering linewidth measurement values.



(A)

(B)

FIGURE IV.1: ORIGINAL AND FILTERED IMAGES OF CCL-EXPOSED GRATING PATTERNS. ORIGINAL IMAGE IS IN (A), WHEREAS THE FILTERED IMAGE IS IN (B). THE BUILT-IN FILTERING ROUTINE WAS FOUND TO IMPROVE THE ANALYSIS ACROSS ALL THE IMAGES.

## 2. EAM exposures

From each EAM exposure, 31 horizontal slices, each 21 vertical pixels wide, were analyzed. Within each slice, the intensity was averaged in the vertical direction to generate a measurement line. One averaged line scan, or slice (labeled 'L1'), is superimposed on top of the related SEM image, shown in Figure IV.2.

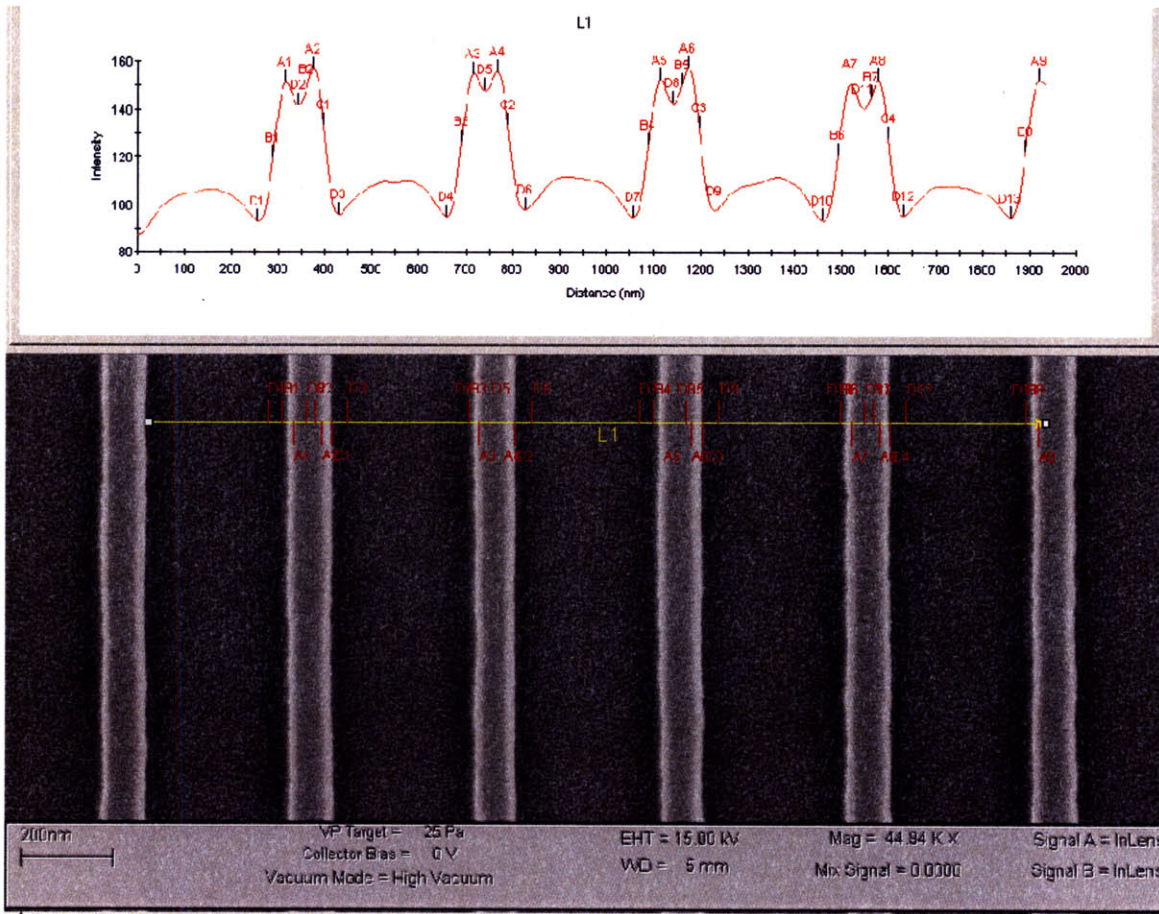


FIGURE IV.2: A REPRESENTATIVE IMAGE UNDERGOING IMAGE PRO ANALYSIS. NOTE THE MARKERS, A, B,C AND D, CORRESPONDING TO RISING INFLECTION, RISING DERIVATIVE EDGE, FALLING DERIVATIVE EDGE AND FALLING INFLECTION RESPECTIVELY. THE AVERAGED LINE, L1, IS SCANNED DOWN THE IMAGE, GENERATING MARKS AND ASSOCIATED X-Y LOCATIONS.

Each measurement line within a picture was then automatically marked for salient intensity features. There were four different mark types: the rising and falling edges of a resist line were used to define the linewidth while the peaks and valleys – on a resist line and cleared space – differentiated the lines from the spaces. Linewidths were then automatically calculated using derivative maxima and minima as well as rising and falling inflection points.

In Matlab, linewidths were extracted between the markers of derivative maxima and minima, (B and C in Figure IV.2), while the inflection points differentiated the lines from spaces.

Linewidths were established for every resist line within each slice of 21 vertical pixels, and standard deviations were taken of all the linewidth measurements on an image. Visually comparing linewidth measurements across an image allowed the removal of bad measurements (Figure IV.3). Finally, the average linewidth and standard deviation were calculated for each image.

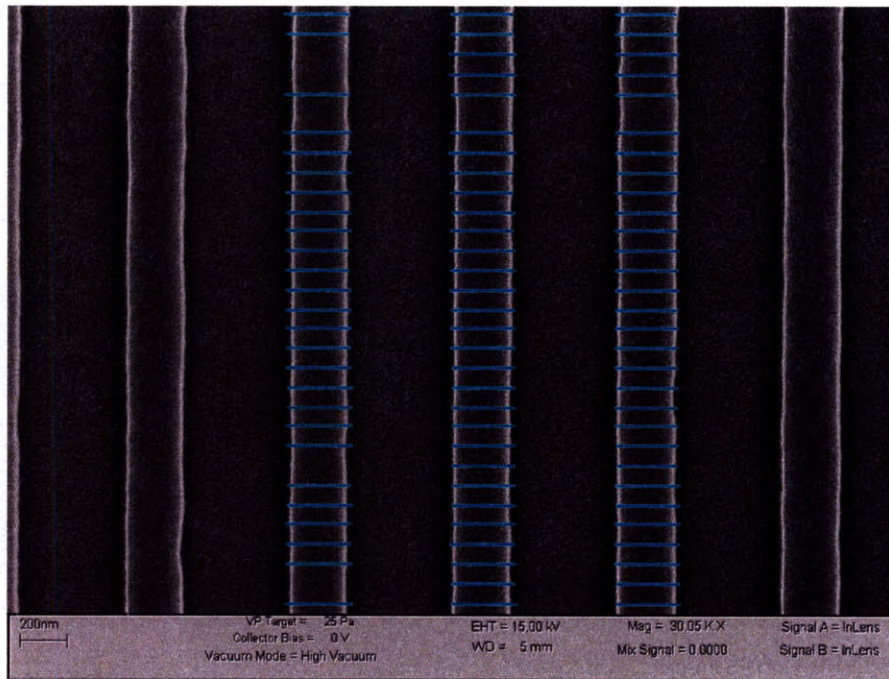
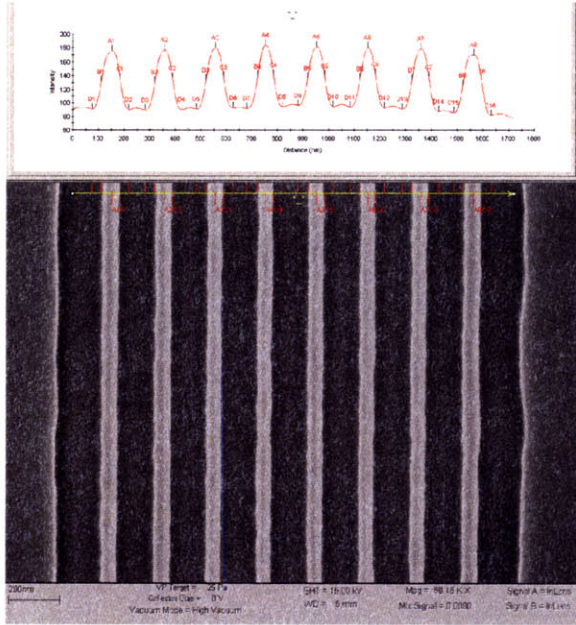
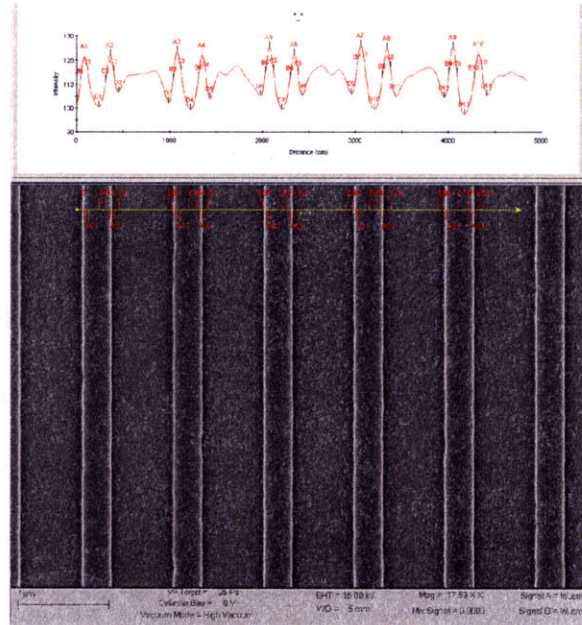


FIGURE IV.3: A REPRESENTATIVE IMAGE UNDERGOING ANALYSIS. THE LINewidthS OVERLAID ON THE IMAGE CAN BE SELECTED AND REMOVED IF THEY ARE INCORRECT. FOR THIS IMAGE, 86 MEASUREMENTS WERE FOUND.

One difficulty arose when analyzing different gratings: the larger gratings had two peaks per line while the smaller gratings had only one as shown in Figure IV.4. This difficulty was addressed by modifying the search algorithm in Matlab to look for different marker patterns. Specifically, the pattern of markers in IV.4A that captures the linewidth between the appropriate (underlined) B and C is DDBACDD, whereas in IV.4B, the pattern changes to DDBACDBACDD.



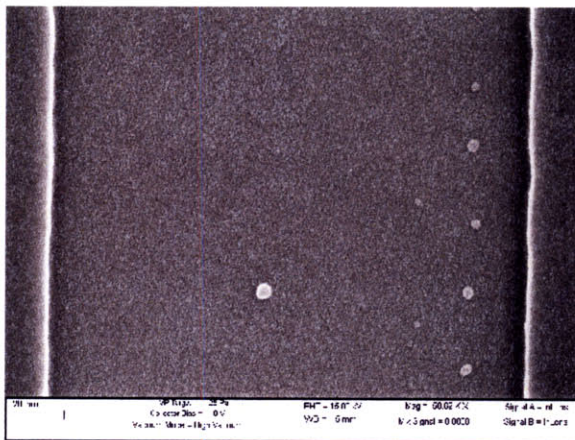
(A)



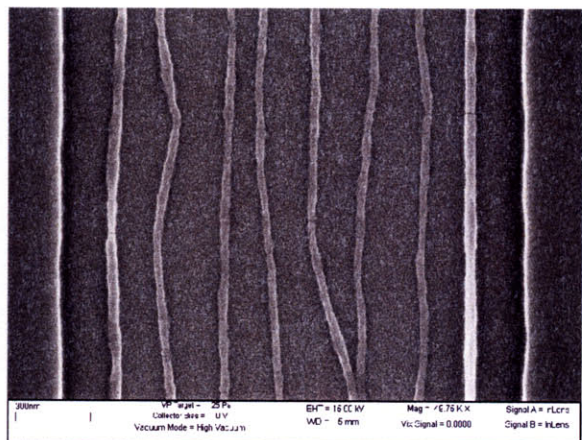
(B)

FIGURE IV.4: THE IMAGE IN (A) WITH NARROW LINES HAS ONLY ONE PEAK AND TWO VALLEYS WITHIN A FULL PERIOD WHILE THE IMAGE IN (B) WITH WIDER LINES HAS TWO PEAKS (VERTICAL WHITE LINES) AND TWO VALLEYS WITHIN A FULL PERIOD. THIS DIFFERENCE REQUIRED TUNING THE AUTOMATED LINewidth MEASUREMENT ROUTINE.

In addition, some of the wafers, when developed and imaged, had poor pattern transfer. Poor transfer examples include when the wafer's grating pattern fully cleared in development (Figure IV.5A) or when the pattern left after development was not a periodic grating (Figure IV.5B).



(A)



(B)

FIGURE IV.5: EXAMPLES OF POOR PATTERN TRANSFER. IN (A), THE RESIST IS CLEARED AND NO MEASUREMENTS WERE POSSIBLE. IN (B), MEASUREMENTS OF THE LINewidth WERE TAKEN THOUGH THE GRATING IS NOT PERIODIC.

If the resist pattern was visible, linewidth measurements were taken on resist lines that appeared to be standing and adhered to the substrate. After collecting the measurements, the

linewidth crossing a resist line was subtracted from the pitch, converting measurements of the distance across a resist line into the distance between resist lines.

### **3. SCM Exposures**

Some unexplained residue was left on the SCM-exposed wafers when they were imaged (Figure IV.6), making it difficult to automatically analyze linewidths in Matlab. Instead, the SCM data was analyzed by hand: instead of using 31 measurement lines (as was done for the EAM), only five manual measurements were analyzed for each filtered SCM grating image. When necessary, to achieve more consistent results, grating image measurements for two marks were averaged. Shown in IV.6 is an SCM-exposed grating with its measurements. The other difference between SCM and EAM exposures, due to the experimental dose range of the SCM, was that more of the smaller features printed better grating patterns. As a result, measurements shown in Figure IV.6 were taken between resist lines rather than across resist lines.

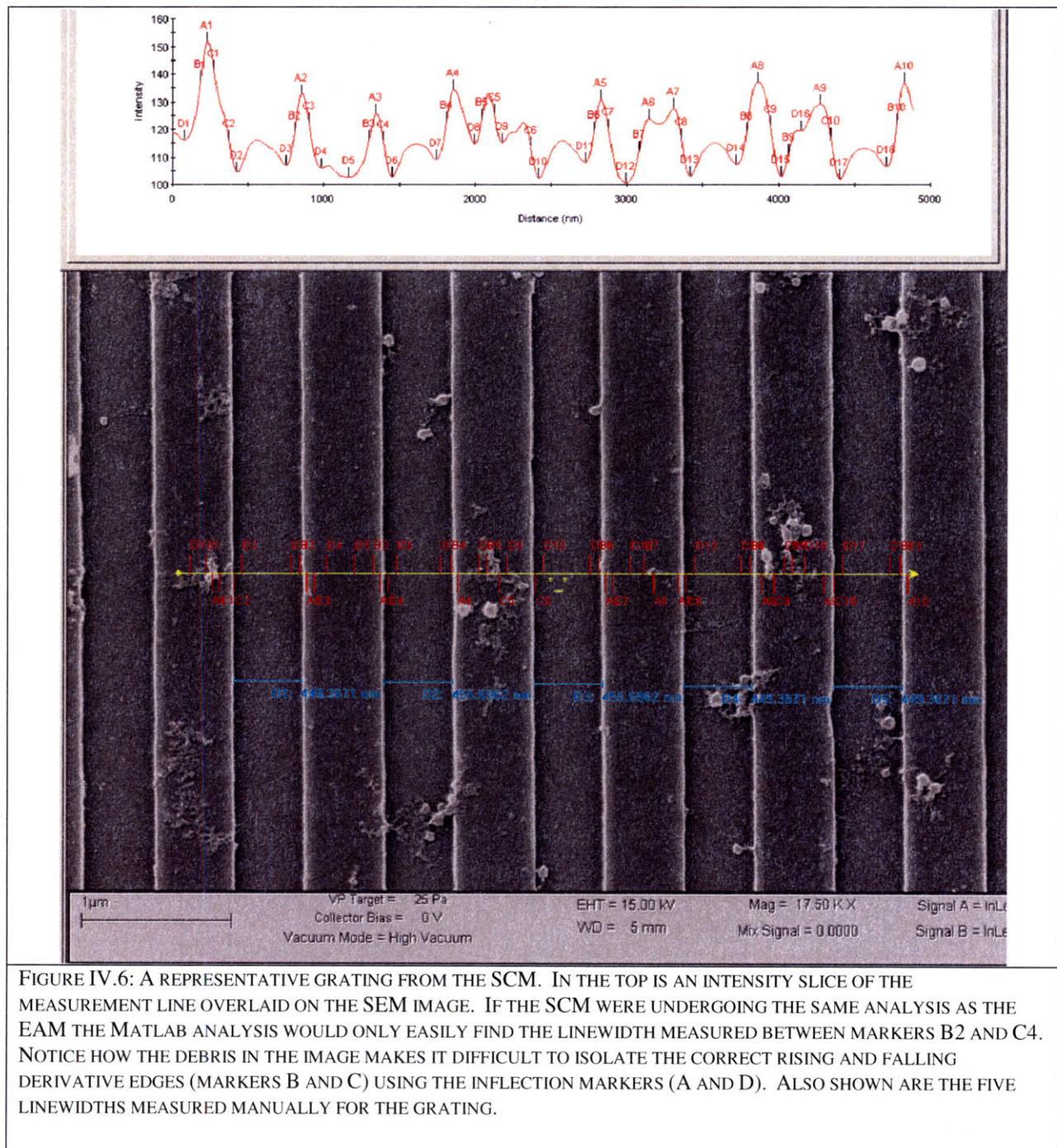


FIGURE IV.6: A REPRESENTATIVE GRATING FROM THE SCM. IN THE TOP IS AN INTENSITY SLICE OF THE MEASUREMENT LINE OVERLAID ON THE SEM IMAGE. IF THE SCM WERE UNDERGOING THE SAME ANALYSIS AS THE EAM THE MATLAB ANALYSIS WOULD ONLY EASILY FIND THE LINewidth MEASURED BETWEEN MARKERS B2 AND C4. NOTICE HOW THE DEBRIS IN THE IMAGE MAKES IT DIFFICULT TO ISOLATE THE CORRECT RISING AND FALLING DERIVATIVE EDGES (MARKERS B AND C) USING THE INFLECTION MARKERS (A AND D). ALSO SHOWN ARE THE FIVE LINewidthS MEASURED MANUALLY FOR THE GRATING.

It should be noted that for the purposes of this thesis the linewidth is defined as the opening in the chrome mask, (*i.e.* the region of high intensity for simulations and the opening in the PMMA for experimental exposures). In cases where the opposite quantity was measured (for

example EAM experimental exposures where the resist width was measured), these measurements were converted to linewidth measurements by subtracting from the design period of the feature.



## V. Linewidth vs Dose Analysis

In this chapter, the effect of dose variations on the linewidth is compared for simulations and experiments using both the SCM and EAM to pattern the trilayer stack.

### 1. Simulation Results

Simulated linewidths of dense grating features on trilayer-stack-coated silicon are plotted against the effective dose,  $D_{\text{eff}}$ , in Figure V.1 for (top) the EAM and (bottom) the SCM. In order to more easily draw useful comparisons between simulations and experiments, the dose in simulated and experimental plots was normalized. To do so, the dose leading to a nominal 150nm linewidth of the 300nm pitched grating is used to normalize the x-axis. So, at a linewidth of 150nm, the unit-less dose is 1. This normalization was done separately for each mask.

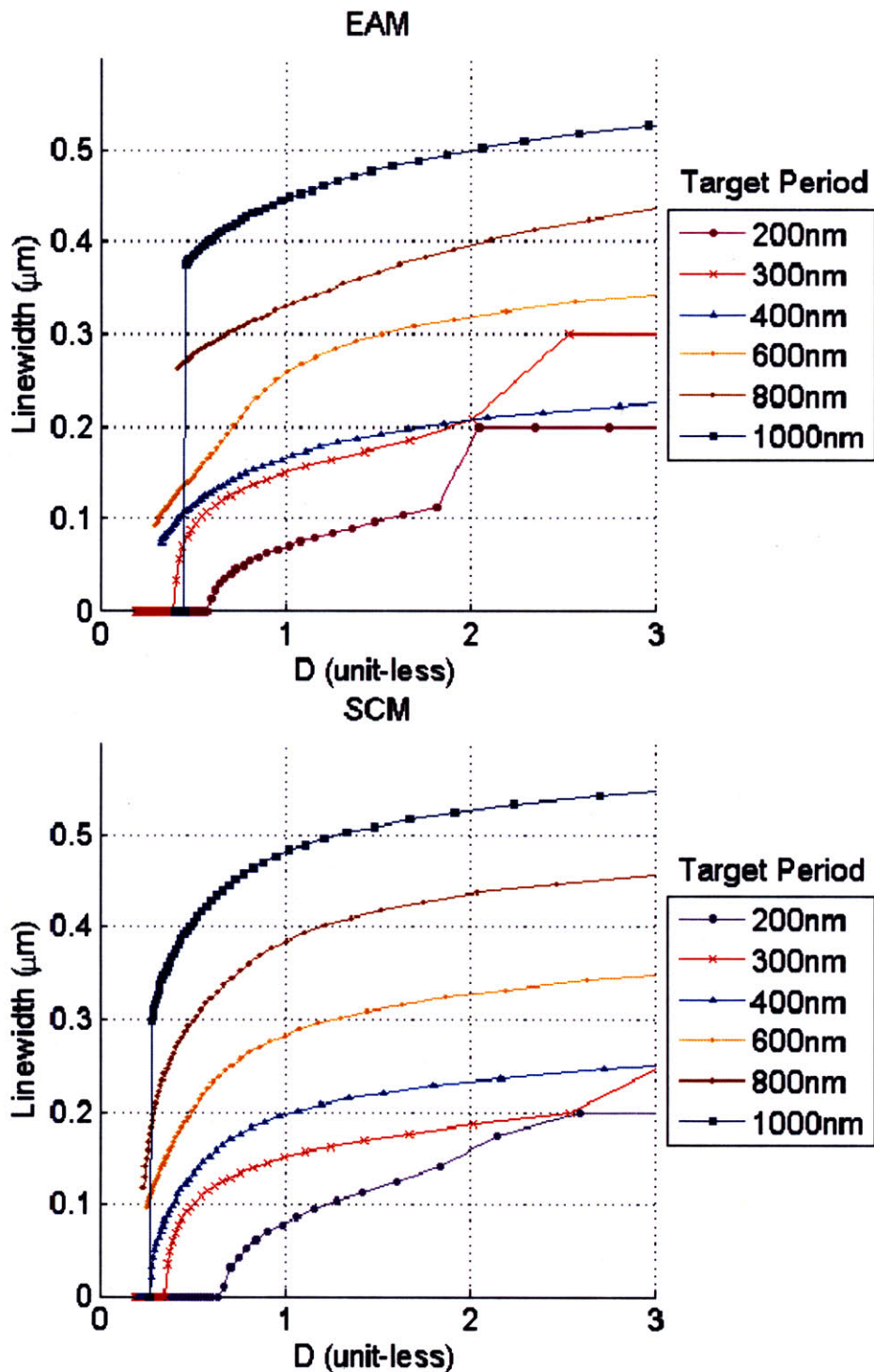


FIGURE V.1: SIMULATED DOSE VERSUS LINewidth FOR GRATINGS OF VARYING PERIOD FOR (TOP) EAM AND (BOTTOM) SCM. THE UNITLESS DOSE IS THE EFFECTIVE DOSE NORMALIZED TO THE 300NM PERIOD GRATING'S NOMINAL DOSE (I.E. THE 300NM GRATING INTERSECTS THE LINewidth OF 150NM AT A NORMALIZED DOSE OF 1). LINewidthS INCREASE WITH DOSE, AS EXPECTED, AND PROCESS LATITUDE APPEARS TO BE REDUCED (I.E. SLOPE OF LINE INCREASES) FOR SMALLER FEATURE SIZES.

Some trends are clear from the plots. As expected, at a higher dose, more resist is developed causing larger linewidths. The required dose to achieve a simulated linewidth of one-half period (the simulated mask linewidth) increases with feature size.

The 200nm and 300nm periods of the EAM simulation have a sharp bend indicating that at the point of measurement the resist developed completely to the simulation boundaries (as discussed in Chapter III).

An analysis of the dose range which yields  $\pm 10\%$  and  $20\%$  variations in the nominal linewidth is presented in Figure V.2. The target linewidth is plotted on the X axis, and the normalized dose on the Y axis. Red stars indicate the simulated dose that yielded the target linewidth. Black dots (connected by dashed lines) indicate the range of simulated doses that gave measured linewidths tolerance within  $\pm 10\%$  and  $20\%$ .

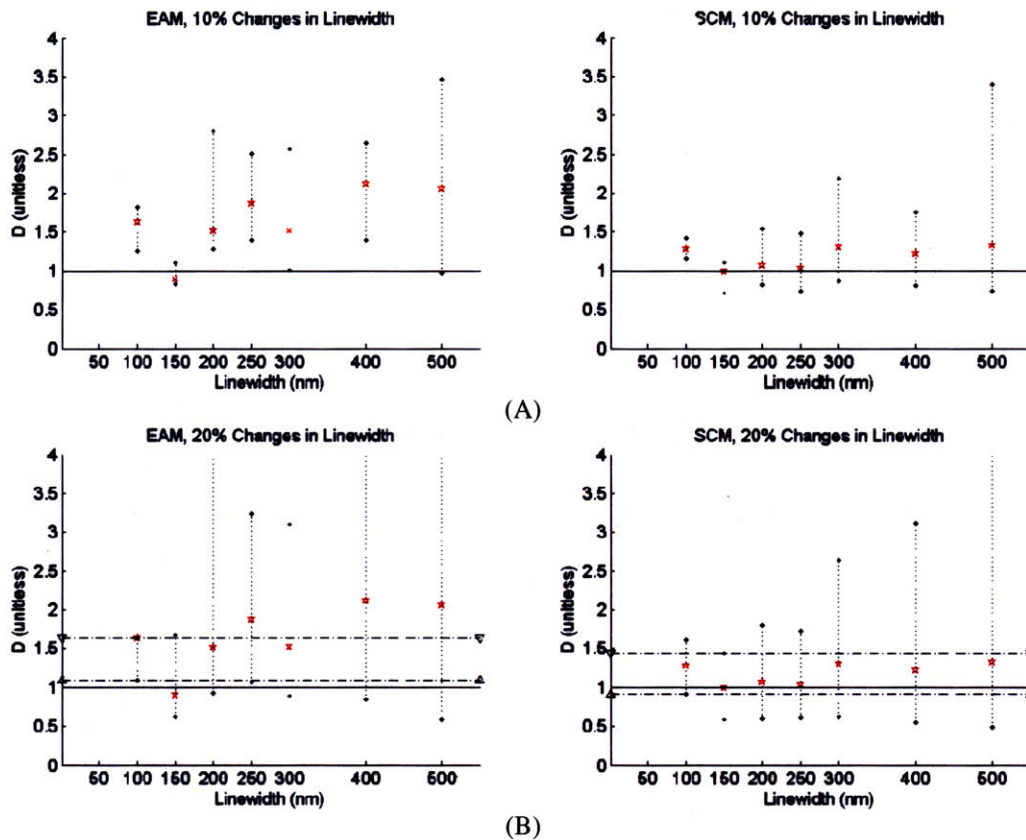


FIGURE V.2: NORMALIZED DOSE (Y AXIS) REQUIRED TO HIT SIMULATED TARGET LINEWIDTHS (X AXIS) FOR LEFT: EAM, RIGHT: SCM. . RED STARS INDICATE THE INTERPOLATED DOSE TO ATTAIN TARGET LINEWIDTH. BLACK DOTS INDICATE RANGE OF DOSES THAT RESULTED IN MEASURED LINEWIDTHS WITHIN TOP (A):  $\pm 10\%$ , BOTTOM (B):  $\pm 20\%$  OF TARGET LINEWIDTH. THE BLACK DASHED HORIZONTAL LINES IN (B) INDICATE "PROCESS WINDOW" FOR THE DOSE YIELDING 20% LINEWIDTH TOLERANCE (SEE TEXT FOR MORE COMPLETE DISCUSSION)

From the plots it is clear that the process latitude (*i.e.* allowable dose variation for linewidth within tolerance specification) decreases with feature size. With the exception of the 150 nm linewidth at a  $\pm 10\%$  specification, which appears to exhibit an anomalously low nominal dose, the simulation results show that target linewidths from 500 nm down to 100 nm are attainable at a single dose with a reasonable process latitude ( $<20\%$  linewidth tolerance). The 150nm and 100nm linewidths limit the process window for both masks. Furthermore, from Figures III.8 and III.9, the EAM 150nm process window (the dotted vertical line above 150nm in V.2A,B) is substantially smaller as a result of the interference discussed in III.8.

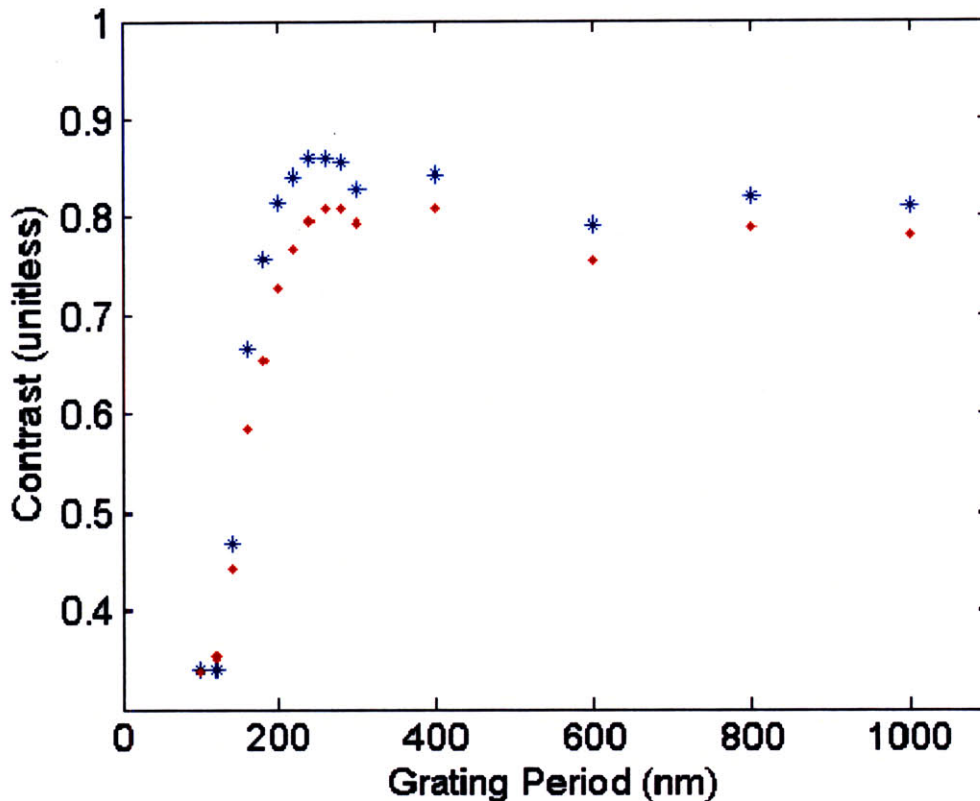
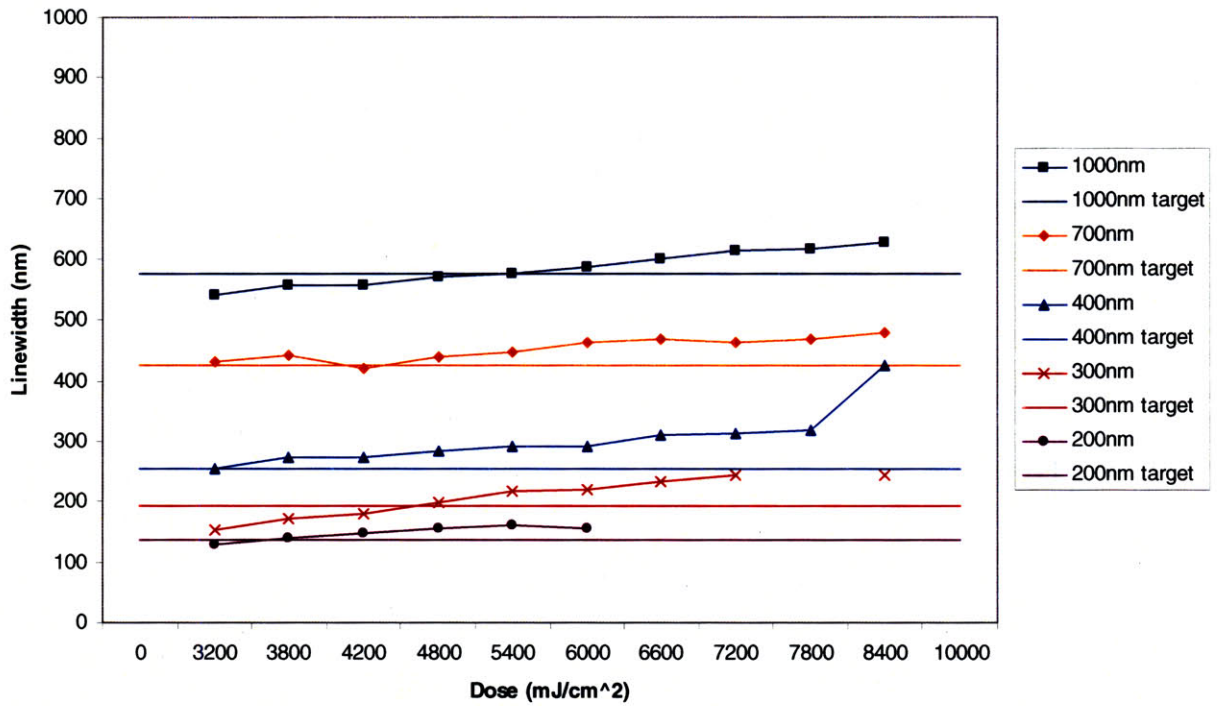


FIGURE V.3: CONTRAST VS. GRATING PERIOD FOR SIMULATED EXPOSURES WITH (BLUE) EAM AND (RED) SCM MASKS. THE EAM CONTRAST REMAINS HIGH TO LOWER GRATING PERIODS

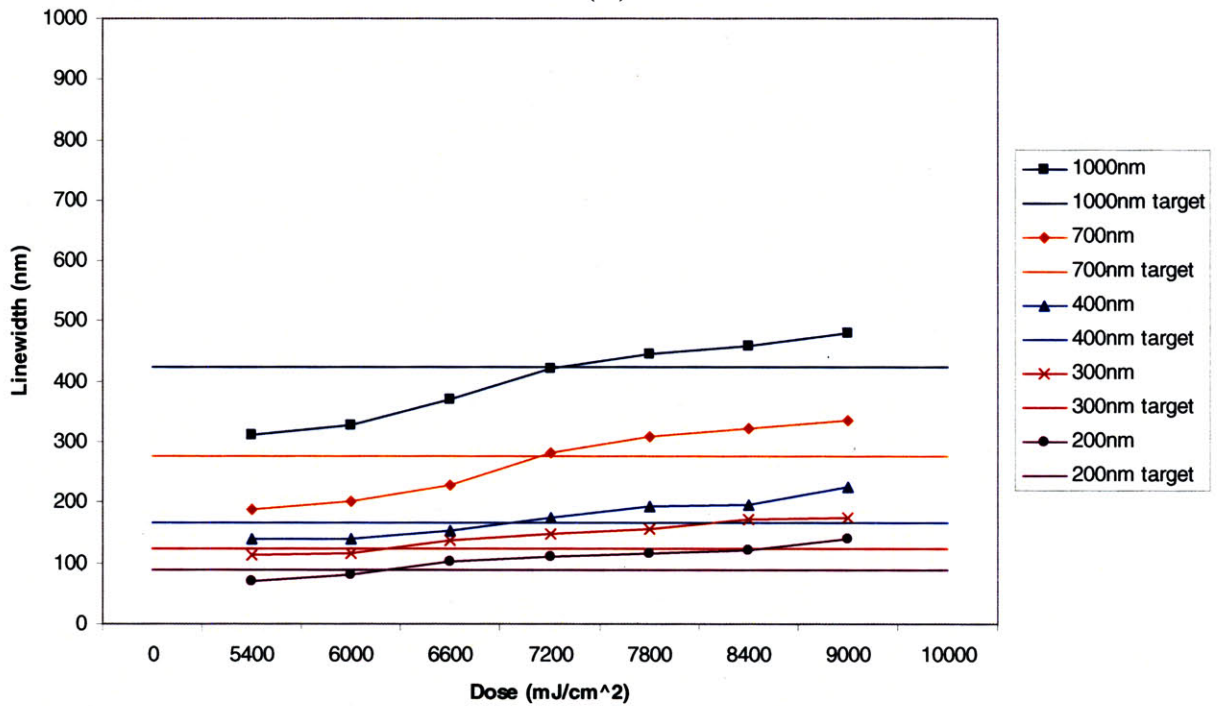
Figure V.3 shows a plot of contrast as a function of simulated grating period for EAM (blue) and SCM (red) masks. The EAM shows higher contrast for all grating periods, but more importantly its higher contrast persists to lower grating periods.

## 2. Experimental results

Figure V.4 shows linewidth vs. dose for experimentally-produced gratings for the EAM (top) and SCM (bottom). Each point on the plot corresponds to one set of measured linewidths for a given mask feature at a given dose. Exposure and analysis details were discussed in Chapter IV. The mask feature size is indicated on the plots by horizontal lines of the same color as the experimental data. As is the case for the simulations, linewidth increases with dose (as expected). Also like the simulations, there appears to be a variation in the dose required to attain the target linewidth with feature size, however, this does not appear to trend in a consistent way.



(A)



(B)

FIGURE V.4: EXPERIMENTALLY-MEASURED LINewidth VS. DOSE FOR GRATINGS OF VARYING PERIOD FOR (A) EAM AND (B) SCM. LINewidthS INCREASE WITH DOSE, AS EXPECTED. UNLIKE THE SIMULATIONS, FOR THE SMALLER GRATINGS PERIODS THERE IS NO APPARENT CHANGE IN THE SLOPE OF THE CURVES WITH LINewidth.

Figure V.5 shows, in a similar fashion to V.2, an analysis of the dose range which yields  $\pm 10\%$  and  $20\%$  variations in the nominal linewidth. The mask linewidth is plotted on the X axis (with dashed vertical lines indicating the designed half-pitch), and the normalized dose on the Y axis<sup>10</sup>. Red stars indicate the exposure dose that yielded the target linewidth. Black dots indicate the range of exposure doses that gave measured linewidths within  $\pm 10\%$  or  $20\%$ . Horizontal dashed lines indicate an acceptable dose range within the specified linewidth tolerance. Lack of dashed horizontal lines indicates that no process window was found.

---

<sup>10</sup> Experimental dose was normalized in a similar fashion to the simulated dose (EAM normalization =  $4200 \text{ mJ/cm}^2$ , SCM =  $7800 \text{ mJ/cm}^2$ ).

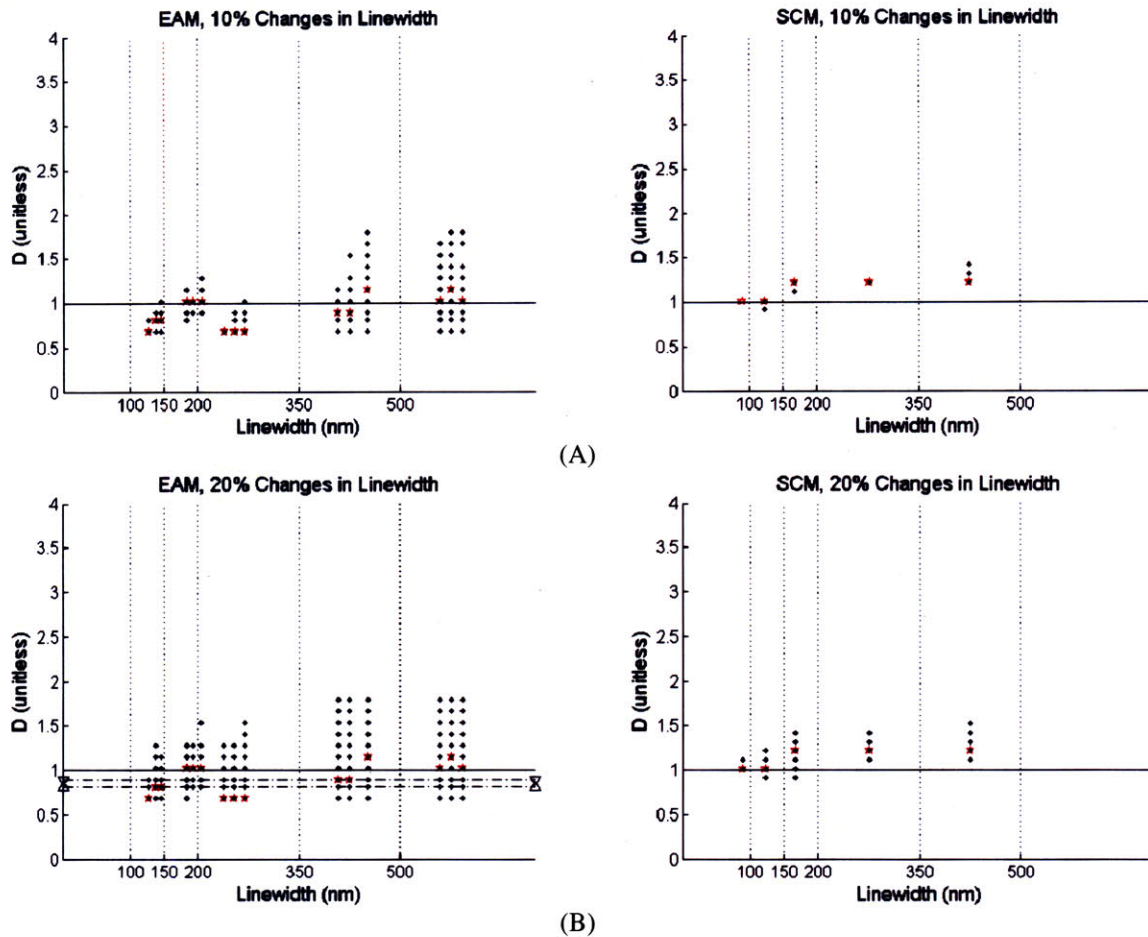


FIGURE V.5: THE EXPERIMENTAL 10% (A) AND 20% (B) PROCESS LATITUDE. LINEWIDTH IS INDICATED ON THE X-AXIS AND THE NORMALIZED DOSE ON THE Y-AXIS. THE DASHED VERTICAL LINES CORRESPOND TO THE HALF-PITCH OF EACH FEATURE. THE STARS ARE THE DOSE CORRESPONDING MOST CLOSELY TO THE MEASURED MASTER LINEWIDTHS OF EACH MASK, WHICH WERE NOT QUITE A 1:1 DUTY CYCLE. THE HORIZONTAL BLACK DASHED LINES (B) FOR THE EAM INDICATE THE PROCESS WINDOW. THE EAM IS THE ONLY MASK THAT SHOWS A PROCESS WINDOW FOR 20% LINEWIDTH VARIATIONS. THE SCM HAS A NARROW PROCESS WINDOW AT 25% LINEWIDTH VARIATION (NOT SHOWN).

From the experimental data it appears, similar to what was seen for simulations, that the process latitude decreases with feature size. Process windows for the EAM show a reasonable dose range suitable for exposing features from ~500 nm down to ~150nm (although there is limited data for some linewidths). Such a window does not appear to exist for the SCM until accepting more than 20% tolerance in linewidth variations.



The simulated and experimental process windows are compared in table V.a for both masks. In general, decreasing the linewidth tolerance yields a smaller process window and in some cases results in *no* process window over all linewidths. If the target linewidth were to exclude the lower target linewidths (100nm and 150nm) then the process window would increase for both masks though more dramatically for the EAM simulations. However, as resolution limits are the focus of this thesis the process window was defined over all the target linewidths.

Another interesting result in Table V.a, the experimental process latitude for the SCM is significantly lower for all linewidth tolerances. Finally, the experimental dose ranges were too coarse to differentiate between some of the linewidth tolerances.

<b>Process Latitude <math>\pm</math> % about Mean Process Window</b>				
Linewidth Tolerance %	EAM		SCM	
	Simulation $\pm$ %	Experimental $\pm$ %	Simulation $\pm$ %	Experimental $\pm$ %
25%	20.20	25.58	24.09	4.35
20%	20.20	5	22.16	0
15%	10.79	5	7.95	Non-existent
10%	12.93	Non-existent	Non-existent	Non-existent

TABLE V.a: THE PROCESS WINDOWS FOR THE EXPERIMENTS AND SIMULATIONS OF THE EAM AND SCM EXPOSURES. THE LINewidth TOLERANCES ARE PRESENTED IN THE LEFT-HAND COLUMN. THE PROCESS WINDOWS IN V.2 AND V.5, AS WELL AS FOR 15% AND 25% LINewidth TOLERANCES, ARE REPRESENTED AS A PERCENTAGE RANGE ABOUT THE MEAN OF THE PROCESS WINDOW. IF NO PROCESS WINDOW EXISTS FOR ALL TARGET LINewidthS THEN THE PROCESS LATITUDE IS NOTED AS NON-EXISTENT.

For process windows limited to larger linewidths (above ~200nm), Figures V.2 and V.5 show clear trends: the process window decreases monotonically along with the feature size, and the dose roughly trends lower with feature size. In contrast, inclusion of smaller (sub-wavelength) features results in a more complicated interpretation of the process latitude. It appears that this relates to interference effects, as indicated in Figure III.8. This highlights the power of using both simulations and experiments to optimize sub-wavelength feature replication. Nonetheless, the EAM appears to exhibit higher process latitude for all feature sizes and tolerances studied in this thesis.

## Summary and Future Work

Background material was presented to motivate the CCL exposure system highlighted by this thesis. Trilayer wafers were designed using EM-Suite to have optimal interlayer thicknesses to minimize back-reflections into the resist. EM-Suite was optimized for FDTD simulation of dense gratings. Masked exposures were performed on trilayer-stack wafers, and simulations were performed to mimic the exposures.

Experiments and simulations confirm that CCL is a suitable technique for patterning features as small as 100 nm with reasonable process latitude. The Process Latitude for the EAM was found to be larger than for the SCM (Figures V.2 and V.5), as would be expected from the higher contrast present for the EAM mask. Intuitively, one can understand this as the SCM contains a region of index  $n = 1$  between the fused silica mask and the PMMA whereas in the EAM this region is filled with high index fused silica. As predicted in Chapter III, lower doses are required to develop using the EAM than are necessary for the SCM (Figure V.4).

This study did not account for registration of multiple masks, though it is currently under investigation. Additionally, the dissolution rate model for DUV irradiated PMMA was not measured and is a topic for future examination.

## VI. Contributions

This thesis suggests an optimal specification of the trilayer stack's interlayer thicknesses for DUV CCL and presents experimental and simulated process latitude study for DUV CCL using trilayer coated wafers patterned by both the SCM and EAM.

## VII. APPENDIX

### 1. Appendix 1: Single Exposure Printing Procedure (adapted from [22])

This appendix presents the step-by-step procedure for performing a print with the LiLCo Systems CCA-M4 Conformable Contact Lithography System.

- Turn on exposure lamp and allow it to warm up (~1 hour).
- Turn on computer and Z-stage control software.
- Set all rocker switches on the remote console to their middle position.
- Turn on POWER and PUMP rocker switches located on the main chassis.
- Move the stage under the exposure lamp
- Measure the power density by manually exposing cardinal locations on the stage.
- Move the dual microscopes to their rear position (if not there already) by pressing the “scopes” rocker switch on the remote console to the EXPOSE position. Put the switch back to its middle position when this is completed.
- Move the stage to the aligner (if not there already) underneath the dual-microscope rails by pressing the “aligner” rocker switch on the remote console to the ALIGN position. Put the switch back to its middle position when this is completed.
- Move the Z-stage back to its original position if it was elevated. Failure to do so may result in damage to the mask and wafer when the mask is put in its holding plate!
- Blow the wafer chuck, wafer back, and wafer front clean with dry, filtered air.
- Place the wafer on the wafer chuck.
- Press the lower-right rocker switch on the remote console to the CHUCK position.

Confirm that the wafer is being held securely in place by gently pushing on the side of the wafer.

- Blow the mask with dry, filtered air
- Place the mask into the mask holder with its pattern absorbers facing down. (Be sure to push the mask towards the rear while doing this such that the mask is contacting the two rear mask retaining clips.)
- Secure the mask in place by pushing the front mask-retaining clip down and back against the mask ring while tightening the clamp screw.
- Press the “contact/release” rocker switch on the remote console to its CONTACT position.
- Adjust the fine contact gauge with the contact-vacuum control located on the remote console until the gauge reads ~2”-3” WC.
- Move the Z-stage up by 200  $\mu\text{m}$  increments until the gauge deflects to the right.
- Adjust the gauge to ~6” WC.
- Press the “contact/release” rocker switch to its RELEASE position.
- Observe the fine release-pressure gauge located on the main control chassis and set the pressure to ~1 mm WC with the release pressure knob to the left of the gauge.
- Bring the Z-stage up by 100  $\mu\text{m}$  and bring the mask into CONTACT. Look for an area of small contact (about the size of a dime).
- If there is no contact point, press the RELEASE the mask and repeat the previous step, otherwise proceed to the next step.
- Note the position of the small contact area and RELEASE the mask.
- Make adjustments to the three mask-height micrometers to center the small contact area. Increasing the values on the micrometers lowers the mask plate.

- Bring the mask back into CONTACT. If the small contact area is still not centered, RELEASE the mask and go back to the previous step. (Leveling the mask may cause a loss of contact with the wafer and require subsequent Z-stage adjustments).
- RELEASE the mask and raise the Z-stage by 50  $\mu\text{m}$
- Bring the mask into CONTACT.
- Slowly increase the contact vacuum until at least 80% of the mask is in intimate contact. (The stage tilt may need adjustments in order to obtain the best possible images).
- Press the “aligner” switch to its EXPOSE position. This will move the aligner head to the exposure lamp.
- Expose the substrate.
- Press the “aligner” switch to its ALIGN position. Move the switch back to its middle position once the aligner head is back underneath the dual-microscopes.
- Slowly reduce the contact vacuum to less than 6” WC.
- RELEASE the mask.
- Lower the Z-stage back to its starting position.
- Loosen the front mask-retaining clip and remove the mask.
- Press wafer-chucking switch to its middle position and remove the wafer.
- Turn off all equipment, allowing the lamp fan 30 minutes to cool the exposure lamp.

## 2. Appendix 2: Simulations of the trilayer stack.

Shown in Figure A2.1 are arrays of simulated intensity profiles with varying linewidth (horizontally) and PMMA thickness (vertically). EAM simulations are shown in A2.1A and SCM simulations are shown in A2.1B. The image scaling in A2.1 is an artifact of EM-Suite; the software displays all plots at the same height, making it appear that the thinner resist has a wider linewidth.

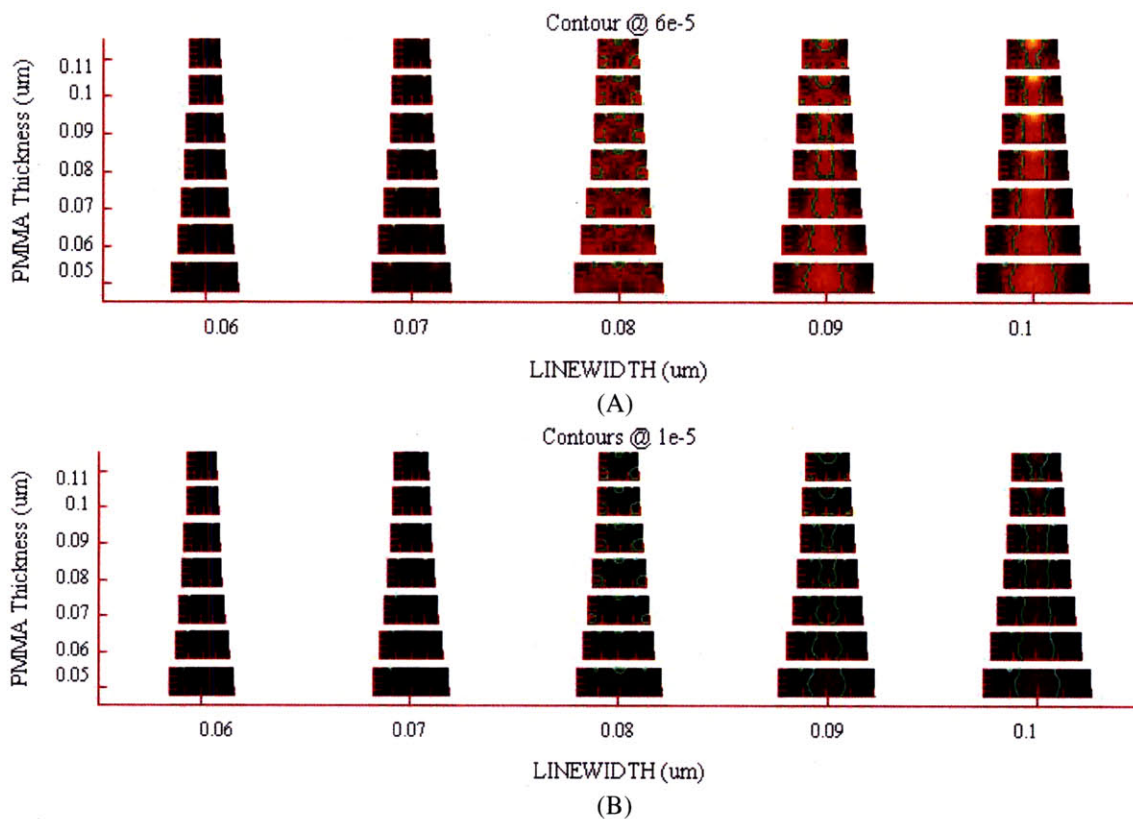


FIGURE A2.1: TRILAYER STACK SIMULATED CCL INTENSITY PROFILES FOR LINEWIDTHS VARYING FROM 60-100 NM AND RESIST THICKNESS VARIED FROM 50-110 NM. A: EMBEDDED AMPLITUDE MASK. B: STANDARD MASK.

In Figure A2.1 the light intensity decreases as it travels deeper into the resist. Note that in A2.1A, the low reflectance is evident in the similar patterns between the pictures displayed in the bottom and top rows: aside from the higher intensity, the upper half of the PMMA resist in the 100nm row is similar in intensity profile to the PMMA resist's profile in the bottom 50nm row. This is also evident in the standard mask figure, A2.1B. Making the resist too thin affects

the planar fabrication process by making it difficult to etch the SiO<sub>2</sub> without eroding the PMMA. As a result, the resist thickness is targeted at 90nm, though in section IV, the PMMA was slightly thicker at 100nm.

Finally, the chrome thickness of the mask was varied. Simulating both the EAM and SCM with chrome lines 20nm, 30nm and 100nm thick generated the plots in Figure A2.2. Notably, when the light is able to penetrate below the aperture the EAM exposed PMMA has straighter contours. Also, the intensity within the PMMA for the 50nm aperture and 20nm chrome absorber layer is less dispersed for the EAM than it is for the SCM, suggesting that smaller resolution limits are attainable with the EAM. Furthermore the thickest chrome lines, excepting the 50nm aperture, (top row of A2.2) of the EAM transmit higher intensities into the PMMA than are transmitted by the SCM. Finally, the intensity of the 50nm aperture, albeit more dispersed, has a higher maximum for the SCM.

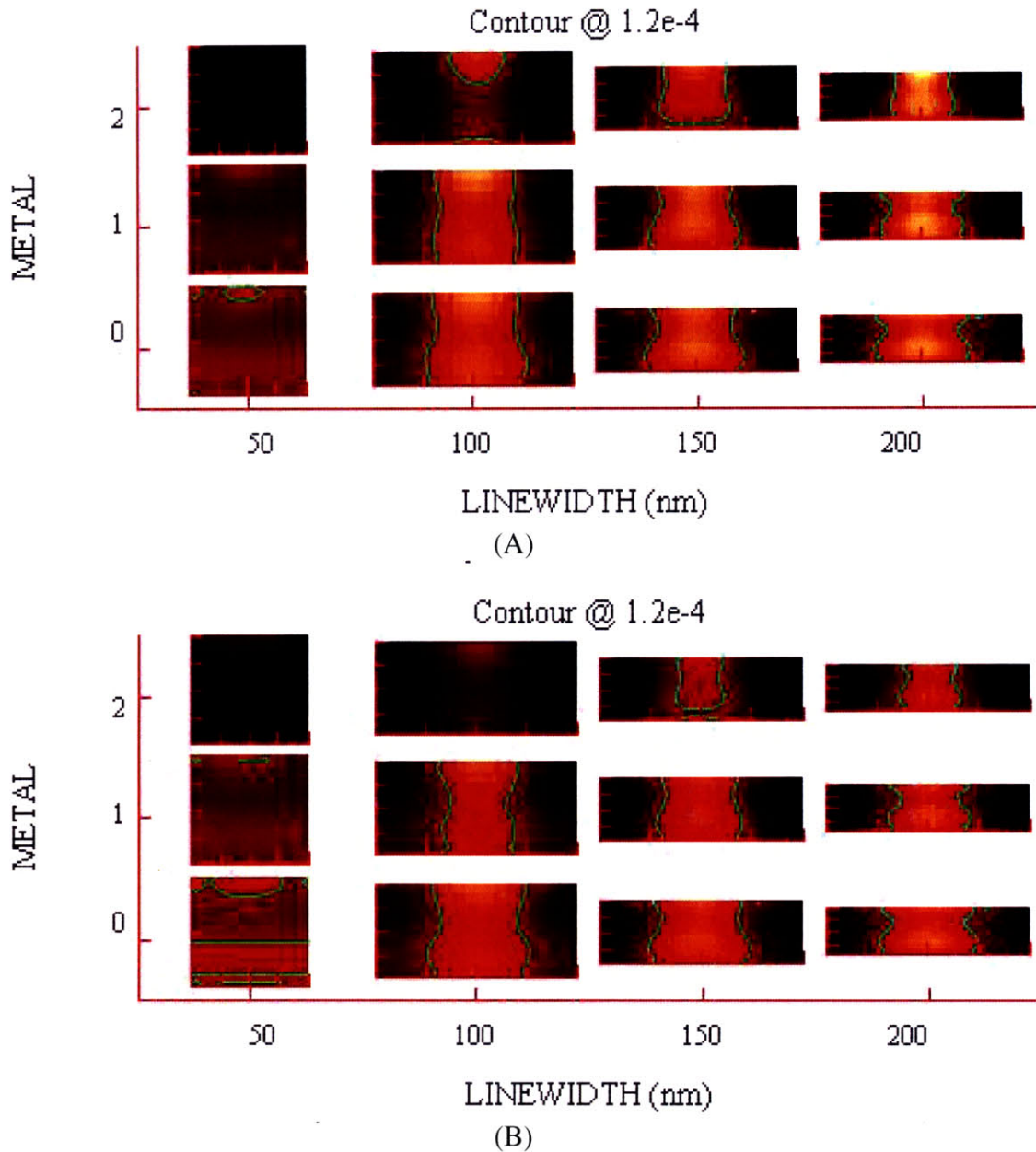


FIGURE A2.2. USING THE OPTIMIZATIONS FROM II AND III: GRATINGS OF  $L[\text{nm}] \in \{50, 100, 150, 200\}$  ARE EXPLORED AS THE THICKNESS OF CHROME  $[ \text{nm} ] \in \{20, 30, 100\}$  IS INCREASED. THE THINNEST CHROME IS IN THE BOTTOM ROW. THE PMMA IS BENEATH THE EMBEDDED MASK IN (A) AND BENEATH THE STANDARD MASK IN (B). NOTE THAT IN (A), THE 50NM COLUMN IS MORE FOCUSED THAN IT IS IN (B): FOR EXAMPLE, THE CONTOUR IS NARROWER .

In figure A2.2, the actual mask specification (courtesy of James Goodberlet) is not used. Instead of using a cell-size of 5nm, the chrome thickness of the mask was chosen to be 20nm in all subsequent simulations [21].



### 3. List of Figures and Tables

- Figure I.1: The Planar fabrication process. During the lithographic step regions of exposed resist are cleared during development. After the lithographic step, the patterned resist undergoes further processing.
- Figure I.2: The LilCo CCL aligner at Draper Laboratory. Arrows indicate the locations of the light source, stage, pneumatic controller and optics controller.
- Figure I.3: The Xe-Hg-arc lamp spectrum as it propagates through the CCL optical system. As the Xe-Hg spectrum (solid green line) is filtered by mirrors (green line with X's), the intensity profile disproportionately decreases in the longer wavelengths (including those beyond the upper limit of this plot), isolating the DUV spectrum for exposures. The incident intensity spectrum multiplied by PMMA absorption (blue line) is shown on the lefthand scale and is discretized into 30 bins, or spectral pairs. The integrated Xe-Hg spectrum is normalized to 1.
- Figure I.4: The layout of the mask. Regions Mark 1, Mark 2 and Mark 3 each contain the 15 gratings in the upper right. In the lower right is the first grating (G2) for the pitch of  $f_3$ . In the matrix of gratings in the upper right, the rows vary in e-beam exposure dose:  $G1=+15\%$ ,  $G2=0\%$  and  $G3=-15\%$  (percentages represent over- or underexposure from nominal 1:1 duty cycle). The columns vary in pitch with  $F1=1000\text{nm}$ ,  $F2=700\text{nm}$ ,  $F3=400\text{nm}$ ,  $F4=300\text{nm}$  and  $F5=200\text{nm}$ .
- Table I.a: Measured linewidths for CCL masks used in this thesis. One mark set per mask was imaged with an (atomic force microscope), and linewidths were measured manually from the AFM image.
- Figure I.5: The imaginary index of refraction of PMMA for the Xe-Hg spectrum between 200 and 260nm. A higher imaginary index of refraction results from more photochemical interactions with the PMMA. (Microchem 950K PMMA measured by J.A. Woollam)
- Figure II.1: (A) reflectance vs wavelength plots for films of  $\text{SiO}_2$  (thickness ranged over 32nm to 98nm) evaporated onto a silicon wafer. The simulated (dotted) and measured (solid) reflectance curves are compared in (B). (B) RMS errors for each  $\text{SiO}_2$  coated wafer is calculated between the experimental and simulated reflectance curves. Note that the error between simulation and experiment was typically less than 5% (with the exception of one wafer, where thickness measurement error is suspected).
- Figure II.2: (A) reflectance vs wavelength plots for ARC-coated wafers. (B) Shows RMS errors between measured and simulated reflectance vs. wavelength for each ARC-coated wafer.

- Figure II.3: The 24 bilayer stack wafers are mapped by their relative film thicknesses into a 6x4 matrix of different SiO<sub>2</sub> and ARC films.
- Figure II.4: (A) Integrated reflectance for bilayer-stack-coated wafers. there are three Data sets of integrated reflectance pictured in this plot. The "poles" sticking up through the surface are the integrated experimental reflectance. The surface is the simulated integrated reflectance over a wide range of film thicknesses, and the contour is the simulated integrated reflectance over the thickness pairs for wafers a-x. (B) RMS error between simulations and measurements of reflectance vs. wavelength (200-300 nm) for 24 bilayer stack wafers. RMS errors are all less than or equal to 11%.
- Figure II.5: Contour plot of integrated total reflectance for the trilayer stack ARC:SiO<sub>2</sub>:PMMA on silicon. the reflectance is integrated over wavelengths from 200nm to 260nm for a range of 13 ARC and 18 SiO<sub>2</sub> thicknesses. The (\*) is the chosen thickness pair at a 70nm thick SiO<sub>2</sub> film and 225nm thick ARC film that minimizes the integrated reflectance to under 1.5% for up to 10nm variations in film thickness.
- Figure III.1: The CCL trilayer stack simulation space for a 100nm linewidth. Within the simulation environment, light is initiated at the excitation plane and propagates through the fused silica mask- see figure I.2, into the absorber layer of chrome lines (in this case 100nm lines:spaces at a 1:2 duty cycle). a vacuum (standard mask) or fused silica (embedded amplitude mask) lies between the chrome Absorber. Light propagating past the absorber layer irradiates the PMMA DUV resist, and reflects off of a layer of silicon dioxide and anti-reflection coating (ARC) and/or a silicon substrate.
- Figure III.2: The best, nominal and worst intensity profiles for variations to the Yee-cell size. Note Pistor's recommended optimal Yee-cell size, or finite difference, is nearest to 8nm. The difference in the simulated intensity does not appear to be significantly different for 4 nm and 8 nm cell sizes, but the simulation degrades significantly for the largest (40 nm) cell size.
- Figure III.3: The root-mean-square error between the best case and other cases of cell size ( $\delta^*$ ), wavelength discretization ( $\lambda^*$ ), and angular discretization ( $\theta^*$ ). The top graph suggests that the simulations are most sensitive to changes in cell size. Next are changes in the number of discrete power spectra. Finally, Changes in angle affect the simulation quality least.
- Table III.a: The simulation environment. The values in this table were found through the optimizations detailed in chapter 2 and the present chapter. The sum of the squared field Amplitudes was normalized to the average measured lamp intensity, 22.4 mW/cm.

- Figure III.4: The simulated resist intensity profiles of the irradiated monolayer (top row) and trilayer (bottom row) stacks using the standard mask. In (A) The x-axis scale is maintained to represent the targeted pitch of each grating. In (B) the X-axis is normalized by the pitch to clarify the intensity profiles of the smaller features.
- Figure III.5: Top and Center: Simulated intensity profiles within the PMMA resist for EAM and SCM for different linewidths. the intensity scale is maintained between all profiles. Bottom: Intensity profile (averaged in Z) for EAM (blue) and SCM (red). note carefully the difference in the profiles between each mask type: Intensity is higher in the resist for EAM, and as the pitch decreases the contrast is maintained to smaller linewidths for the EAM.
- Figure III.6: Simulated intensity in the PMMA of a 420nm pitch trilayer stack exposure using the EAM. (A) Shows the simulated resist intensity profile (mask linewidth indicated by blue dashed lines). (B) Depicts the contour that intersects the mask linewidth (210 nm) halfway up the resist (z = 595nm). (C) Depicts the nominal contour corresponding to the averaged intensity at the mask linewidth as Z ranges from 587nm to 623nm. Notice the slight difference between the contour in (B) and (C). The Asymmetry of the contours is a numerical artifact from EM-Suite.
- Figure III.7: Contours are drawn for the nominal intensity and  $\pm 50\%$ .
- Figure III.8: Simulated intensity within the PMMA resist above the trilayer stack. The contours in each image, moving outward from the center of the resist, begin at the intensity corresponding to the target linewidth through the center of the resist. The remaining contours are at 80%, 60%, 50% and 40% of the nominal intensity. In A, the 50% and 60% contours penetrate the resist horizontally capping the measured linewidth (from the center of the resist) that extends beyond the simulation space to 300nm. The same is not true of the contours in B.
- Figure III.9: (A) Linewidth vs. Intensity level for the simulated 420 nm period exposure shown in previously in III.8,9. The nominal intensity,  $I_0$  gives a linewidth closest to the mask linewidth. As expected, the linewidth decreases with increasing intensity. The data in (A) is transformed into linewidth vs. dose in (B) by assuming a clipping model for development where intensities greater than the nominal intensity develop out completely. Furthermore, the intensity variations are transformed into dose (see text).
- Figure IV.1: Original and filtered images of CCL-exposed grating patterns. Original Image is in (A), whereas the filtered image is in (B). The built-in filtering routine was found to improve the analysis across all the images.
- Figure IV.2: A representative image undergoing Image Pro analysis. Note the markers, A, B,C and D, corresponding to rising inflection, rising derivative edge, falling derivative edge and falling inflection respectively. The averaged line, L1, is scanned down the image, generating marks and associated x-y locations.

- Figure IV.3: A representative image undergoing analysis. The linewidths overlaid on the image can be selected and removed if they are incorrect. For this image, 86 measurements were found.
- Figure IV.4: The image in (A) with narrow lines has only one peak and two valleys within a full period while the image in (B) with wider lines has two peaks (vertical white lines) and two valleys within a full period. This difference required tuning the automated linewidth measurement routine.
- Figure IV.5: Examples of poor pattern transfer. In (A), the resist is cleared and no measurements were possible. In (B), measurements of the linewidth were taken though the grating is not periodic.
- Figure IV.6: A representative grating from the SCM. In the top is an intensity slice of the measurement line overlaid on the SEM image. If the SCM were undergoing the same analysis as the EAM the Matlab analysis would only easily find the linewidth measured between markers B2 and C4. Notice how the debris in the image makes it difficult to isolate the correct rising and falling derivative edges (markers B and C) using the inflection markers (A and D). Also shown are the five linewidths measured manually for the grating.
- Figure V.1: Simulated Dose versus linewidth for gratings of varying period for (top) EAM and (Bottom) SCM. The unitless dose is the effective dose normalized to the 300nm period grating's nominal dose (*i.e.* the 300nm grating intersects the linewidth of 150nm at a normalized dose of 1). Linewidths increase with dose, as expected, and process latitude appears to be reduced (*i.e.* slope of line increases) for smaller feature sizes.
- Figure V.2: Normalized dose (Y axis) required to hit simulated target linewidths (X axis) for Left: EAM, Right: SCM. . red stars indicate the interpolated dose to attain target linewidth. Black dots indicate range of doses that resulted in measured linewidths within Top (A):  $\pm 10\%$  and Bottom (B):  $\pm 20\%$  of target linewidth. The gray boxes indicate the dose window that yields linewidths within the specification for all feature sizes (except 150 nm  $\pm 10\%$ , which appears to have an anomalously low target dose).
- Figure V.3: Contrast vs. grating period for simulated exposures with (blue) EAM and (red) SCM masks. The EAM contrast remains high to lower grating periods
- Figure V.4: Experimentally-measured linewidth vs. dose for gratings of varying period for (A) EAM and (B) SCM. Linewidths increase with dose, as expected. Unlike the simulations, there is no apparent change in the slope of the curves with linewidth.
- Figure V.5: The experimental 10% (A) and 20% (B) process Latitude. The dashed lines correspond to the half-pitch of each feature. The stars are the dose corresponding

most closely to the measured master linewidths of each mask. For the EAM, each grating, G1-G3, is shown if it is within the processing window for the measured master linewidths. In contrast, the (hand-measured) SCM gratings are only presented for one grating set (G2). The Process window is largest for the EAM mask in both (A) and (B).

Figure A2.1: Trilayer stack simulated CCL intensity profiles for linewidths varying from 60-100 nm and resist thickness varied from 50-110 nm. A: embedded amplitude mask. b: standard mask.

Figure A2.2. Using the optimizations from II and III: Gratings of  $L[\text{nm}] \in \{50,100,150,200\}$  are explored as the thickness of chrome  $[\text{nm}] \in \{20,30,100\}$  is increased. The thinnest chrome is in the bottom row. the PMMA is beneath the Embedded mask in (A) and beneath the standard mask in (B). Note that in (A), the 50nm column is more focused than it is in (B): for example, the contour is narrower .

#### 4. REFERENCES

- [1] Plummer, J., Deal, M., Griffin, P., *Silicon VLSI Technology*. Prentice Hall, New Jersey, 2000. Chapter 2.
- [2] Fox, R., Isaacs, L. and Stokes, S., "Photolytic Degradation of Poly(methyl Methacrylate)." *Journal of Polymer Science: part A*, **1**, 1079 (1963)
- [3] Mimura, Y., Ohkubo, T., Takeuchi, T. and Sekikawa, K., "Deep UV Photolithography." *Japanese Journal of Applied Physics*, **17**, 541 (1978)
- [4] Lin, B., "Deep UV Lithography." *Journal of Vacuum Science and Technology*, **12**, 1317 (1975)
- [5] Choi, J., Moore, J., Corelli, J., Silverman, J. and Bakrhu, H., "Degradation of Poly(methyl Methacrylate) by Deep Ultraviolet, X-ray, Electron Beam, and Proton Beam Irradiations." *Journal of Vacuum Science and Technology*, **B6**, 2286 (1988)
- [6] Schattenburg, M., Aucoin, R. and Fleming, R., "Optically Matched Trilevel Resist Process for Nanostructure Fabrication." *Journal of Vacuum Science and Technology*, **B13**, 3007 (1995)
- [7] White, J., Craighead, H., Howard, R., Jackel, L., Behringer, R., Epworth, R., Henderson, D. and Sweeney, J., "Submicron, Vacuum Ultraviolet Contact Lithography with an F<sub>2</sub> Excimer Laser." *Applied Physics Letters*, **44**, 22 (1984)
- [8] Smith, H., "Method for Fabricating High Frequency Surface Wave Transducers." *Review of Scientific Instruments*, **40**, 729 (1969)
- [9] Baylies, W., *Semiconductor Products and Solid State Technology*, Cowan Publishing Corp., New York, 1981, p.132
- [10] Bracken, R., *VLSI Electronics, Vol.6*, edited by N. Einspruch, Academic Press, New York, 1983, p.295
- [11] Japanese Patent 58,28,739, *Chemical Abstract*, **100**, 183203 (1983)
- [12] Smith, H., "Fabrication Techniques for Surface-Acoustic-Wave and Thin-Film Optical Devices." *Proceedings of the IEEE* **62**, 1361 (1974)
- [13] Chou, S., Krauss, P. and Renstrom, P., "Imprint Lithography with 25-Nanometer Resolution." *Science, New Series*, **272**, 85 (1996)
- [14] Zhao, X., Xia, Y. and Whitesides, G., "Soft Lithographic Methods for Nano-Fabrication." *Journal of Material Chemistry*, **7**, 1069 (1997)
- [15] Carter, D., Smith, H., Rhee, K. and Marrian, C., "Sub-40nm Pattern Replication with  $\pm 20\%$  Process Latitude by Soft Contact X-ray Lithography." *SPIE Conference on Emerging Lithographic Technologies III*, **3676**, 277 (1999)
- [16] Smith, H., Efremow, N. and Kelly, P., "Photolithographic Contact Printing of 4000Å Linewidth Patterns." *Journal of the Electrochemical Society: Solid-State Science and Technology*, **121**, 1503 (1974)

- [17] Smith, H., Bachner, F. and Efremow, N., "A High Yield Photolithographic Technique for Surface Wave Devices." *Journal of the Electrochemical Society* **118**, 821 (1971)
- [18] Melingailis, J., Smith, H. and Efremow, N., "Instrumentation for Conformable Photomask Lithography," *IEEE Trans. Electron Devices* **ED-22**, 496 (1975)
- [19] Goodberlet, J., "Patterning 100 nm Features Using Deep-Ultraviolet Contact Photolithography." *Applied Physics Letters*, **76**, 667 (1999)
- [20] Goodberlet, J. and Kavak, H., "Patterning Sub-50 nm Features with Near-Field Embedded-Amplitude Masks." *Applied Physics Letters*, **81**, 1315 (2002)
- [21] Paulus, M., Schmid, H., Michel, B. and Martin, O.J.F., "Contrast Mechanisms in High-resolution contact Lithography: A Comparative Study." *Microelectronic Engineering*, **57-58**, 109, (2001)
- [22] Sakai, M., "Fabrication Process Changes for Performance Improvement of a RF MEMS Resonator: Conformable Contact Lithography, Moire Alignment, and Chlorine Dry Etching," Masters Thesis, Draper Laboratory, June 2005.
- [23] LilCo, Melrose, MA 781-665-1480
- [24] Lin, B. "Deep-UV Conformable-Contact Photolithography for Bubble Circuits." *IBM Journal of Resist Development*, 213 (1976)
- [25] Moreau, W.M., "Contact and proximity print." *Semiconductor Lithography*, Plenum Press, New York, 1988, Chapter 8-3.
- [26] Oral Communications, *Micro- and Nano-Engineering*, Barcelona September 17-20, 2006, p. 55, 65
- [27] Hawryluk, R.J., Smith, H., Soares, A. and Hawryluk, A. "Energy Dissipation in a Thin Polymer Film by Electron Beam Scattering." *Journal Applied Physics*, **46**, 2528, (1975)
- [28] Walsh, M., Hao, Y., Ross, C. and Smith, H. "Optimization of a Lithographic and Ion Beam Etching Process for Nanostructuring Magnetoresistive Thin Film Stacks." *Journal of Vacuum Science and Technology*, **B18**, 3539 (2000)
- [29] Staelin, D., Morgenenthaler, A. and Kong, J. "Non-normal Incidence in Lossy Media," *Electromagnetic Waves*. Prentice Hall, New Jersey, 1998, Chapter 4
- [30] Pistor, T.V., "Electromagnetic Simulation and Modeling with Applications in Lithography," PHD Thesis at University of California, Berkley, Memorandum No. UCB/ERL M01/19, May 1, 2001. [Online] Available from Panoramic Technology, [www.panoramictech.com](http://www.panoramictech.com)
- [31] Pistor, T.V. "Accuracy Issues in the Finite Difference Time Domain Simulation of Photomask Scattering." [Online] Available from Panoramic Technology, [www.panoramictech.com](http://www.panoramictech.com)
- [32] Widmann, D. and Stein, K.U., "Semiconductor Technologies of Reduced Dimensions," *Proceedings Of the 2<sup>nd</sup> European Solid State Circuits Conference*; CEP Consultants Ltd.:Edinburgh, Scotland, **29**, 1977, (1976)

- [33] Alkaisi, M.M., Blaikie, R.J. and McNab, S.J., "Nanolithography in the evanescent near field," *Adv. Mater.* **13**, 877 (2001). Invited review paper.